

TABLE OF CONTENTS

Table of Contents	i
	Page
Introduction	1
1 High energy nuclear physics	3
1.1 Standard model	3
1.1.1 Quantum chromodynamics	5
1.1.2 Parton distribution functions	9
1.1.3 QCD phase diagram	13
1.2 Relativistic heavy-ion physics	15
1.2.1 History of heavy-ion accelerators	15
1.2.2 Geometry of nucleus-nucleus collisions	17
1.2.3 Evolution of heavy-ion collisions	19
1.2.4 Experimental probes of the QGP	21
2 Experimental setup	33
2.1 Experimental setup	33
2.1.1 Large Hadron Collider	33
2.1.2 CMS detector	33
2.1.3 Trigger System	33
2.1.4 Object reconstruction	33
3 Charmonia	35
3.1 Theory	35
3.2 Analysis	35
3.3 Results	35
4 W BOSON PRODUCTION IN PROTON-LEAD COLLISIONS	37

TABLE OF CONTENTS

4.1	Theory	38
4.1.1	History of weak theory	38
4.1.2	Electroweak theory	41
4.1.3	Nuclear PDF	43
4.1.4	PDF global fits	44
4.1.5	Production of W bosons at LHC	47
4.2	W boson production in pPb collisions at $\sqrt{s_{\text{NN}}} = 8.16$ TeV	51
4.2.1	Observables	51
4.2.2	Comparison with theoretical models	53
4.2.3	Comparison with other LHC experiments	55
5	Conclusion	59
	Bibliography	61
	List of Tables	73
	List of Figures	75

INTRODUCTION

HIGH ENERGY NUCLEAR PHYSICS

This chapter introduces the concepts of high energy nuclear physics relevant for the analysis of the production of W bosons and J/ψ mesons in heavy-ion collisions. The elementary particles and fundamental interactions of the standard model are described in Section 1.1. In addition, the extreme state of hot dense hadronic matter known as the Quark-Gluon Plasma (QGP) and the study of its properties in heavy-ion collisions is reviewed in Section 1.2.

1.1 Standard model

The standard model (SM) is a theoretical framework that describes the properties of elementary particles and their interactions. The SM was developed during the 20th century through the collaborative effort of many physicists. According to the SM, all matter in the universe is composed, at the most fundamental level, of elementary particles called fermions. Fermions are particles with half-integer spin which behave according to Fermi-Dirac statistics formulated by Enrico Fermi [1] and Paul Dirac [2] in 1926. As a consequence, fermions are restricted by the Pauli exclusion principle [3] which dictates that two or more fermions with the same quantum numbers cannot occupy the same quantum state.

In addition, fermions can be classified as leptons or quarks. There are six leptons arranged in three "generations": the electron (e^-) and the electron neutrino (ν_e), the muon (μ^-) and the muon neutrino (ν_μ), and the tau (τ^-) and the tau neutrino (ν_τ).

The neutrinos are electrically neutral and almost massless, while the other leptons have negative electric charge (-1) and sizeable masses. In the case of quarks, there are six "flavours" paired also in three generations of increasing mass. The up and down quarks belong to the first generation, while the more heavier quarks are included in the second generation (charm and strange quarks) and third generation (top and bottom quarks). The up (u), charm (c) and top (t) quarks have positive electric charge (+2/3) while the down (d), strange (s) and bottom (b) quarks have negative electric charge (-1/3). Each quark also carry another quantum number called colour charge that can have three different values labelled as red, green and blue. Moreover, each fermion has an associated antiparticle with the same mass but with opposite charges. The positron (e^+) is the antiparticle of the electron, while the name of the rest of antiparticles simply starts with the prefix "anti" (e.g. anti-quarks \bar{q} , anti-neutrinos $\bar{\nu}$ or anti-leptons ℓ^+).

The interactions between fermions are described in the standard model by three fundamental forces: electromagnetism, strong nuclear force and the weak nuclear force. The gravitational force is currently not included in the SM but the effect of gravity at the quantum level is so small that it is considered negligible. In the SM, each fundamental force is mediated by the exchange of integer spin particles called bosons that follows the Bose-Einstein statistics proposed in 1924 by Sateyndra Bose [4] and Albert Einstein [5].

The electromagnetic and the weak nuclear forces are described in the SM by the electroweak theory. The electromagnetic interactions between particles with electric charge are mediated by photons which are massless and chargeless spin one particles. On the other hand, the weak interactions can act on all fermions but the strength of the weak force is roughly 10^{-5} weaker than the electromagnetic force. The weak interactions are mediated by three massive vector bosons: the electrically charged W^\pm bosons and the electrically neutral Z boson. Processes involving neutrinos or the change of quark flavour are only possible through weak interactions. Moreover, the strong nuclear force is responsible for the interactions between colour charged particles (i.e. quarks) described by the theory of Quantum Chromodynamics (QCD). The strong interactions are mediated by spin one bosons called gluons which carry colour and anti-colour charge. Thus, unlike the photon, gluons can interact with themselves confining the quarks in colourless configurations known as hadrons. Hadrons compose of three (anti-)quarks are called baryons while those made of a quark and an anti-quark are called mesons. Exotic hadrons containing four and five quarks have been recently observed by the Belle [6] and LHCb [7] collaborations, respectively.

The generation of mass of the elementary particles is explained in the SM by the

Brout-Englert-Higgs (BEH) mechanism [8, 9]. The weak bosons and the fermions acquire their mass by interacting with the Higgs field. The stronger a particle couples to the Higgs field, the more massive it becomes. The interaction with the Higgs field is mediated by a scalar boson, the so-called Higgs boson. The BEH mechanism was experimentally confirmed after the CMS [10] and ATLAS [11] collaborations announced the discovery of the Higgs boson in 2012. The basic properties of leptons, quarks and bosons of the SM are summarized in Table 1.1.

	Name	Symbol	Mass	Charge	Spin	Interactions	
Quark	1 st	Up	u	2.2 MeV	2/3	1/2	All
		Down	d	4.7 MeV	−1/3	1/2	All
	2 nd	Charm	c	1.28 GeV	2/3	1/2	All
		Strange	s	96 MeV	−1/3	1/2	All
	3 rd	Top	t	173.5 GeV	2/3	1/2	All
		Bottom	b	4.18 GeV	−1/3	1/2	All
Lepton	1 st	Electron	e^-	511 keV	-1	1/2	Electroweak
		Electron neutrino	ν_e	< 2 eV	0	1/2	Weak
	2 nd	Muon	μ	106 MeV	-1	1/2	Electroweak
		Muon neutrino	ν_μ	< 2 eV	0	1/2	Weak
	3 rd	Tau	τ	1.78 GeV	-1	1/2	Electroweak
		Tau neutrino	ν_τ	< 2 eV	0	1/2	Weak
Boson		Photon	γ	< 10 ^{−18} eV	0	1	Electromagnetic
		Gluon	g	0	0	1	Strong
		W boson	W [±]	80.4 GeV	±1	1	Electroweak
		Z boson	Z	91.2 GeV	0	1	Electroweak
		Higgs boson	H	125.1 GeV	0	0	BEH mechanism

Table 1.1: Basic properties of quarks, leptons and bosons from the SM. The table includes the mass, electric charge, spin and type of interactions of each particle. The values are taken from Ref. [12]

1.1.1 Quantum chromodynamics

The development of new experimental techniques, such as the synchrocyclotron and the bubble chamber, led to the discovery of many hadronic resonances during the 1950s and 1960s. In an attempt to organize these new hadrons, Murray Gell-Mann [13] and Yuval Ne'eman [14] proposed in 1961 the Eightfold Way classification. The Eightfold Way scheme managed to sort the hadrons into representations of the SU(3) group leading to

the creation of the quark model. The quark model, developed in 1964 by Gell-Mann [15] and George Zweig [16], considered the hadrons as composite objects made of valence quarks and anti-quarks. Even though the quark model was succesful at describing the properties of most hadrons known at the time, it had problems explaining the structure of the Ω^- baryon. The Ω^- baryon is made of three strange quarks with parallel spins but such configuration was forbidden by the Pauli exclusion principle. To solve the spin-statistics paradox, Oscar Greenberg [17] proposed that each quark also carried a 3-valued quantum number named the colour charge. The description of the strong interactions using the concept of colour charges was formally developed in the theory of QCD by Harald Fritzsch, Heinrich Leutwyler and Murray Gell-Mann [18] in 1973.

Quantum chromodynamics is a non-abelian quantum field theory with gauge symmetry group SU(3), that describes the strong interactions between colour charged particles. The primary objects of QCD are the quarks which carry one colour charge (e.g. green) and the gluons which carry a colour and an anti-colour charge (e.g. red-antiblue). There are eight different gluons which form an octet representation of SU(3). The lagragian of QCD is:

$$L_{QCD} = \sum_f \bar{q}_{f,i} \left(i\gamma^\mu D_\mu^{i,j} - m_f \delta^{a,b} \right) q_{f,j} - \frac{1}{4} F_{\mu,\nu}^a F_a^{\mu,\nu} \quad (1.1)$$

where g_s is the strong gauge coupling constant, and γ^μ are the Dirac γ -matrices. The $q_{f,i}$ represents the Dirac spinor of a quark with flavour f , mass m_f and colour index i running from $i = 1$ to 3. The QCD gauge covariant derivative $D_\mu^{i,j}$ and the gluon field strength tensor $F_{\mu,\nu}^a$ are given by:

$$\begin{aligned} D_\mu^{i,j} &= \delta^{i,j} \partial_\mu - i \frac{g_s}{2} \lambda_a^{i,j} G_\mu^a \\ F_{\mu,\nu}^a &= \partial_\mu G_\nu^a - \partial_\nu G_\mu^a + g_s f_{bc}^a G_\mu^b G_\nu^c \end{aligned} \quad (1.2)$$

where f_{bc}^a are the SU(3) structure constants, $\lambda_a^{i,j}$ are the Gell-Mann matrices, and G_μ^a is the vector field of a gluon with index a that runs from $a = 1$ to 8.

Expanding the terms in Eq. (1.1), one can derive three different types of vertices representing the interaction between quarks and gluons, and the gluon self-interactions as shown in Fig. 1.1.

1.1.1.1 Running coupling constant

In quantum field theory, physical quantities are calculated by performing a perturbative expansion of the theory in terms of its coupling constant. The first order of the expansion

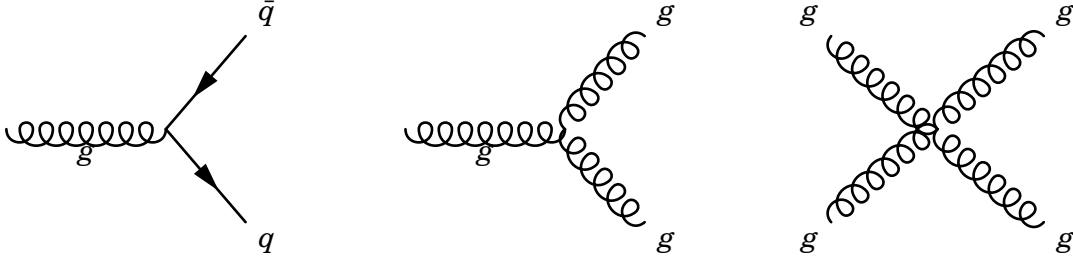


Figure 1.1: Feynman diagrams of the QCD vertices for quark-gluon coupling (left), triple gluon self-coupling (middle) and quadri gluon self-coupling (right).

is called the leading order (LO). At higher orders, some of the terms contain loops (infinite integrals) which diverge due to high momentum particles in the loop (ultraviolet divergence). The ultraviolet (UV) divergences can be removed from the perturbation series by renormalizing the Lagrangian.

The renormalization procedure consist of replacing the bare parameters of the Lagrangian by finite renormalized parameters, and then treat the divergences by applying a regularization scheme. There are many regularization schemes but one of the most often used is the Minimal Subtraction (MS) scheme based on dimensional regularization. The MS scheme consists on solving the loop integrals in d arbitrary spacetime dimensions introducing a scale μ in the process [19]. In order to keep the physical observables independent of the renormalization scale, the dependence of the renormalized paramaters on the scale μ is fixed by renormalization group equations (RGE) [19].

In the case of QCD, the strength of the strong interactions is parametrized by the strong coupling constant $\alpha_s = 4\pi g_s^2$. The UV divergences in perturbative QCD (pQCD) appears from loop diagrams like those shown in Fig. 1.2.

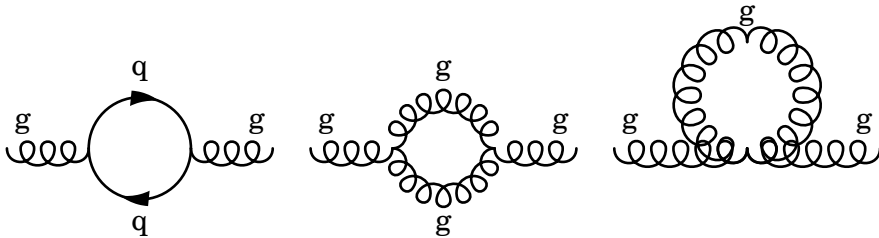


Figure 1.2: Feynman diagrams of 1-loop contributions to pQCD.

The renormalized strong coupling constant $\alpha_s(\mu^2)$ satisfies the following RGE [12]:

$$\mu^2 \frac{d\alpha_s(\mu^2)}{d\mu^2} = \beta(\alpha_s) = -\alpha_s^2 (\beta_0 + \beta_1 \alpha_s + \dots) \quad (1.3)$$

where $\beta_0 = 7/(4\pi)$ and $\beta_1 = 13/(8\pi^2)$ are the 1-loop and the 2-loop coefficients of the β -function, respectively [12]. In the one-loop approximation, $\alpha_s(\mu^2)$ can be expressed as:

$$\alpha_s(\mu^2) = \frac{1}{\beta_0 \ln\left(\frac{\mu^2}{\Lambda_{\text{QCD}}^2}\right)} \quad (1.4)$$

where Λ_{QCD} is the QCD Landau pole (i.e. the scale at which the coupling becomes infinite). The factorization scale μ is generally associated to the energy scale Q of a given process. This means that $\alpha_s(\mu^2)$ is not really a constant but depends on the energy scale, so it is also known as the QCD running coupling constant. Fig. 1.3 presents the latest results on the measurement of $\alpha_s(Q^2)$ as function of the energy scale Q [12].

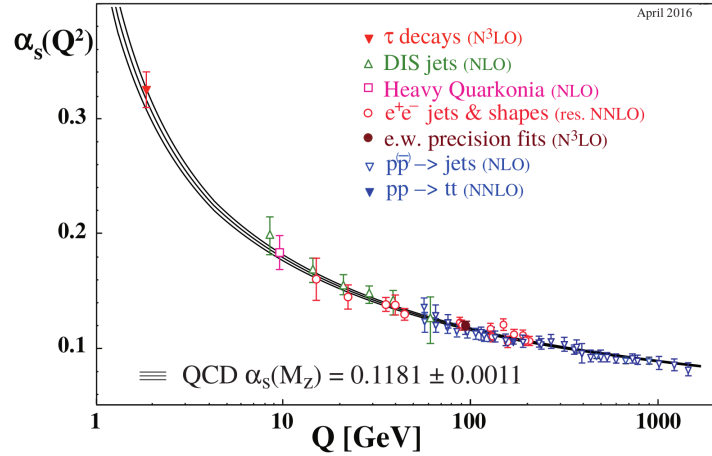


Figure 1.3: Summary of measurements of α_s as a function of the energy scale Q . Figure taken from the PDG [12]

1.1.1.2 Asymptotic freedom

One important consequence of the non-abelian nature of QCD is the asymptotic freedom of colour charged particles discovered in 1973 by David Gross and Frank Wilczek [20], and also by David Politzer [21]. As can be observe in Fig. 1.3, the strength of the strong nuclear force gets asymptotically reduced as the energy scale is increased. Perturbative QCD can then be fully applied in the asymptotic free regime since the strong coupling constant is small.

Considering the inverse relation between the wavelength of particles and their momentum (de Broglie hypothesis [22]), asymptotic freedom implies that the strong nuclear interactions between quarks gets weaker at larger momentum or at shorter distances. This phenomenon can be understood qualitatively as derived from the interaction with the QCD vacuum. The presence of virtual quark-antiquark pairs from the vacuum acts as colour dipoles reducing (screening) the strength of the colour charge field. In addition, virtual gluons can couple to other gluons increasing (antiscreening) the net effect of the colour charge seen at larger distances. Thus, there is an interplay between quark-antiquark pair colour screening and gluon colour antiscreening, where the later effect dominates in QCD.

1.1.1.3 Colour confinement

The fact that quarks and gluons have never been observed isolated in normal conditions is due to another phenomenon of QCD called colour confinement. The intensity of the strong nuclear force increases when the energy scale is reduced or the distance is increased as seen in Fig. 1.3. The large strong interactions between colour charged particles force the quarks and gluons to be confined in hadrons. The divergent behaviour of α_s at the Landau pole shown in Eq. (1.4), is a consequence of the inability of pQCD to describe the low energy regime which becomes non-perturbative. An alternative way to study the low energy regime is to use Lattice QCD calculations.

The strong nuclear force can be described qualitatively as a string. When a quark and anti-quark gets separated, the gluon string that mediates their strong interaction elongates increasing the energy. The string eventually breaks when it becomes more energetically favorable to create a light quark-antiquark pair, splitting the original meson into two mesons as shown in Fig. 1.4. This leads to a process called hadronization where quarks and gluons produce a cascade of hadrons. The presence of colour charged particles in high energy collisions can be measured experimentally using jets derived by clustering the final state hadrons in narrow cones.

1.1.2 Parton distribution functions

The production of particles in hadronic collisions depends on the evolution of the partons (i.e. quarks and gluons) inside the hadrons and the parton momentum transfer during the hard scattering. Since the strong coupling constant decreases with increasing momentum scales, partons can be considered asymptotically free within the hadron during collisions

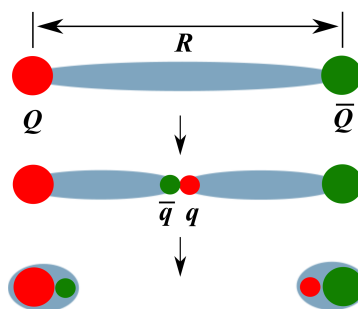


Figure 1.4: Sketch of the gluon string breaking between a quark Q and an anti-quark \bar{Q} due to $q\bar{q}$ pair creation. Figure taken from Ref. [23]

involving large momentum transfer. In this case, each parton carries a fraction of the total momentum of the hadron, represented by the quantity called Bjorken x [24] (labelled simply as x), given by:

$$p_{parton} = x p_{proton} \quad (1.5)$$

The quantum properties of the hadrons, such as the electric charge or spin, are derived from the valence quarks. The interaction between valence quarks is mediated by the exchange of gluons. Gluons can also produce virtual quark-antiquark pairs and other gluons through self interactions. The virtual quarks produced inside the hadrons are called sea quarks. The gluons and sea quarks do not contribute to the quantum numbers of the hadrons but they play a key role in the interaction of hadrons with other particles.

A convenient way of studying the evolution of partons within hadrons is through the parton distribution functions (PDFs). The PDF of a hadron represents the probability that a parton carries a given fraction x of the total momentum of the hadron.

According to the QCD factorization theorem, the cross section of a given hard scattering process in hadronic collisions can be factorized into a partonic cross section times the PDFs of each incoming hadron. The advantage of the factorization theorem is that the partonic cross section can be derived using perturbative QCD and does not depend on the colliding hadrons. On the other hand, the PDFs can not be currently calculated from first principles due to the non-perturbative nature of QCD, but they can be determined from global fits to experimental data since the PDFs are independent of the initial scattering process (i.e. universal). The hadronic cross section in a given final state can be expressed at LO, using the factorization theorem, as:

$$\sigma_{h_1, h_2} = \sum_{f_1, f_2=(q, \bar{q}, g)} \int_0^1 dx_1 dx_2 f_1^{h_1}(x_1, Q^2) f_2^{h_2}(x_2, Q^2) \hat{\sigma}_{f_1 f_2} \quad (1.6)$$

where Q^2 is the momentum scale, $f^{h_1}(x, Q^2)$ is the PDF of a given incoming hadron h_1 , and $\hat{\sigma}_{f_1 f_2}$ represents the partonic cross section of the scattering process between partons f_1 and f_2 .

The Q^2 scale dependence of the PDFs is described by the parton evolution equations developed by Dokshitzer, Gribov, Lipatov, Altarelli and Parisi (DGLAP) [25–27]. In the DGLAP formalism, the PDFs can be expressed in terms of kernels $P_{q_1 q_2}$ (called splitting functions), and the evolution equations of the parton densities can be written as:

$$\begin{aligned} \frac{d}{dt} q_i(x, t) &= \frac{\alpha_s(Q)}{2\pi} [q_i \otimes P_{qq} + g_i \otimes P_{qg}] \\ \frac{d}{dt} g(x, t) &= \frac{\alpha_s(Q)}{2\pi} \left[\sum_i (q_i + \bar{q}_i) \otimes P_{gq} + g_i \otimes P_{gg} \right] \\ [q \otimes P] &= \int_x^1 d\epsilon \frac{q(\epsilon, t)}{\epsilon} \times P\left(\frac{x}{\epsilon}\right) \end{aligned} \quad (1.7)$$

where $t \propto \text{Log}(Q^2)$, and $P_{q_1 q_2}$ represents the probability of finding a parton q_1 in another parton q_2 . In other words, the DGLAP evolution equations state that the PDF of a given parton q at an x value is determined from the contribution of all the partons at higher momentum fraction considering their probability of decaying into the parton q .

From the definition of the PDFs, one can also formulate a set of structure functions defined as:

$$F_2^p(x) = \sum_q e_q^2 f(x, Q^2) x \quad (1.8)$$

where e_q is the electric charge of a given quark flavour q . The structure functions were extensively measured in Deep-Inelastic Scattering (DIS) collisions at the Hadron-Elektron-Ringanlage (HERA) accelerator. The DIS process consists on the inelastic scattering of electrons off protons as presented in Fig. 1.5. In the DIS process, the momentum transferred from the electron to the proton is defined as $Q^2 = -q^2 = -(k - k')^2$ and the corresponding Bjorken x fraction is $x = Q^2/(2p \cdot q)$.

The measurements of the F_2 structure function performed by the ZEUS collaboration [28] at HERA are shown in Fig. 1.6. Even though DIS experiments were not able to probe the gluons directly, the DIS data showed that valence quarks did only carry half of the proton momentum been the other half carried by the gluons.

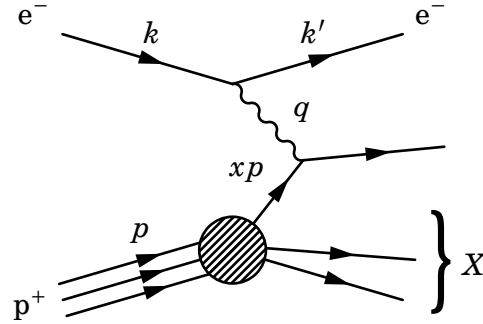
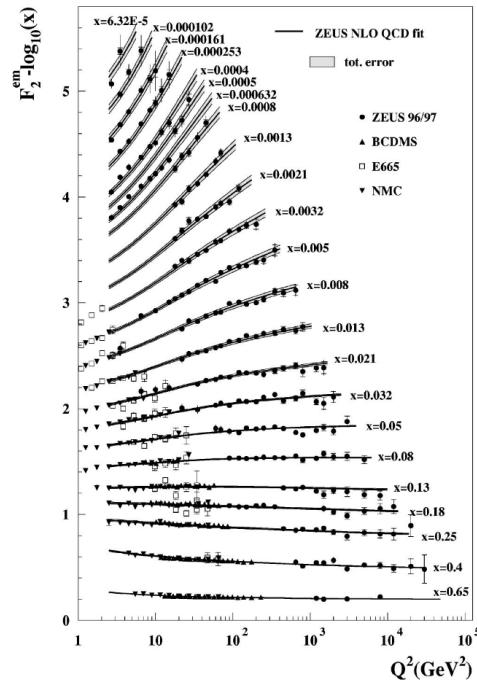


Figure 1.5: Feynman diagram of deep inelastic scattering of electrons against protons


 Figure 1.6: NLO QCD fits to the to the ZEUS F_2 structure function data from 1996, 1997 and proton fixed-target at HERA. The error bands of the fit represent the total experimental uncertainty from both correlated and uncorrelated sources. Figure taken from Ref. [28]

Another important process used to constrain PDFs is the production of electroweak bosons such as W bosons or Drell-Yan (DY). In the DY process, a quark from one hadron and an anti-quark from another hadron annihilate into a virtual photon (γ^*) or Z boson which then decays to a pair of leptons as shown in Fig. 1.7. The measurement of DY production can be used to constrain the quark PDFs in a wide range of momentum fraction x depending on the invariant mass of the dilepton pair. In addition, the measurement of the production of positive and negative charged W bosons in hadronic collisions is used to disentangle the flavour dependence of the quark PDFs. More details about the W boson production will be provided in Chapter 4.

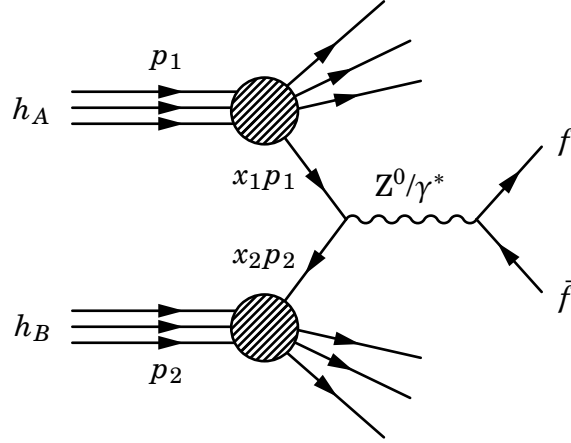


Figure 1.7: Feynman diagram of neutral charged Drell-Yan process

1.1.3 QCD phase diagram

The first attempt to describe the temperature dependence of matter at high energies was performed by Rofl Hagedorn in 1965 [29]. Hagedorn considered matter at high energies as a gas made of hadrons and employed a thermodynamical bootstrap approach to describe the hadron gas. After studying the mass spectrum of all the hadron species measured at the time, Hagedorn realized that the density of hadron species grows exponentially until it diverges at a temperature $T_H \approx 158$ MeV, known as the Hagedorn temperature. Years later, with the advent of QCD, it was understood that the Hagedorn temperature described a transition from a hadron gas to a state of matter where quarks and gluons are asymptotically free called the Quark Gluon Plasma (QGP).

The description of the QCD phase transition turned out to be complicated because the critical temperature was close to the QCD scale $\Lambda_{\text{QCD}} \approx 255 \text{ MeV}$ [30], where perturbative calculations are no longer reliable. An alternative method to study the non-perturbative regime of QCD consists of solving numerically the QCD field equations on a discrete space-time grid using a method called Lattice QCD. Nowadays, lattice QCD is able to describe the evolution of matter at finite temperatures and low densities. A sketch of the QCD phase diagram in terms of the temperature T and the baryon chemical potential μ_B ¹ is shown in Fig. 1.8.

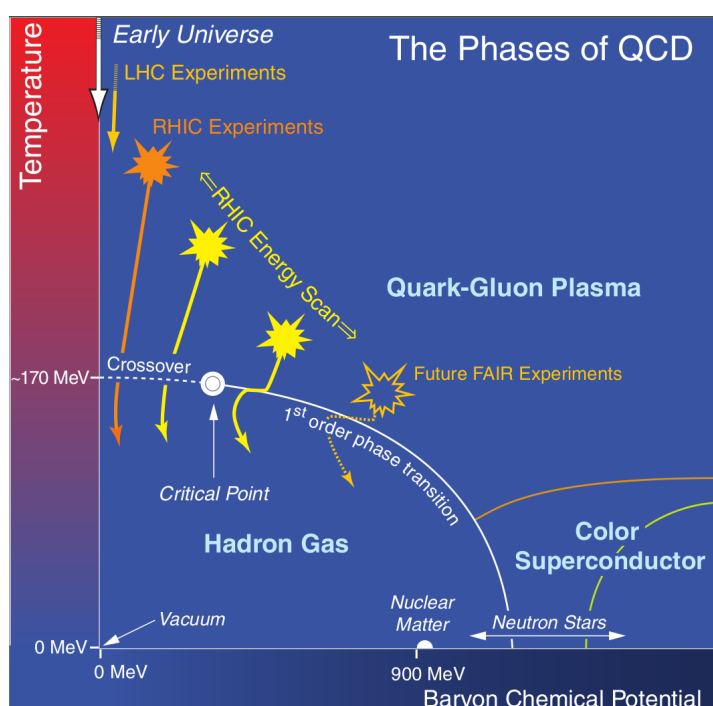


Figure 1.8: Schematic of the QCD phase diagram for nuclear matter. The solid lines show the phase boundaries and the solid circle represents the critical point. Figure taken from Ref. [31]

Normal matter exists in nature at low temperatures. At higher densities, matter undergoes a phase transition to a degenerate gas of fermions known as neutron gas, which is present in dense stellar objects such as white dwarfs or neutron stars. It is theorized that at even higher densities matter could reach a state of colour superconductivity where quarks bind together into Cooper pairs [32]. On the other hand, matter present at the beginning of the universe or produced in TeV-scale particle collisions has very

¹The baryon chemical potential can be viewed as a measure of the excess of matter over anti-matter.

low baryon chemical potential. At $\mu_B = 0$, matter is described at low temperatures as a hadron gas and it becomes a QGP when the temperature exceeds the critical point. The phase transition between the hadron gas and the QGP has been established, using lattice QCD, to be a crossover where the two states coexist [33, 34].

1.2 Relativistic heavy-ion physics

Heavy-ion colliders have become essential tools to explore the fundamental properties of matter. Collisions of nuclei are used to probe the phase transitions of QCD and to recreate the QGP in the laboratory. The QGP is believed to have existed at the beginning of the Universe and to be part of the core of some astrophysical objects such as neutron stars. The study of the QGP allows to test QCD in the most extreme regimes and provides an insight on the evolution of the Universe. Some of the primary research goals of the heavy-ion physics programme is to understand the formation and properties of the QGP, and how does matter interact with the nuclear medium. Nowadays, the experimental study of ultra-relativistic (i.e. at energies above $\sqrt{s_{NN}} > 10$ GeV) heavy-ion collisions is performed at the Brookhaven National Laboratory (BNL) and at the European Organization for Nuclear Research (CERN).

1.2.1 History of heavy-ion accelerators

The interest in probing the QCD phase diagram in the laboratory arose in the 1970s after Werner Scheid, Hans Müller and Walter Greiner predicted that nuclear matter could be compressed in heavy-ion collisions at nucleus-nucleus energies larger than 100 MeV/nucleon [35]. The shock compression mechanism could reach matter densities up to five times higher than the density of atomic nuclei ($\rho_0 = 0.16$ baryons/fm³) [35]. Coinciding in time, the Lawrence Berkely Laboratory (LBL) decided to transform their proton synchrotron accelerator Bevatron into a heavy-ion experiment called Bevalac. Heavy ions were produced in the Bevalac using the heavy-ion linear accelerator Super-HILAC and then sent to the Bevatron where the ions were further accelerated against a fixed target with energies of up to 2.6 GeV/nucleon [36]. The goal at the time was to investigate the equation of state (EoS) of hadronic matter at high densities. The understanding of the relation between the pressure and the energy density of dense matter was a key element needed to describe the dynamics of astrophysical objects such as supernovae and neutron stars [37, 38].

The successful creation of compressed nuclear matter at the Bevatron motivated the construction of several heavy-ion accelerators at higher energies. The first one was the Alternating Gradient Synchrotron (AGS) particle accelerator at the Brookhaven National Laboratory (BNL). The AGS became the first facility in 1960 to accelerate protons to an energy of 33 GeV, which allowed to discover the muon neutrino in 1962, to observe the CP violation of the weak interactions in Kaon decays in 1964, and to discover the J/ψ meson in 1974. An electrostatic accelerator called the Tandem Van de Graaf was built in 1970 to provide beams of ions to the AGS. The relativistic heavy-ion programme started at AGS in 1986 and lasted for 12 years during which several experiments were performed (e.g. E802, E858, E866, E896 and E917). AGS accelerated Si beams at 14.6 GeV/nucleon and Au beams at 11.1 GeV/nucleon, and collided them against different types of fixed targets (e.g. Al and Au).

In addition, CERN built the Super Proton Synchrotron (SPS) in 1976. To study the QGP, CERN added an Electron-Cyclotron Resonance (ERC) ion source in 1986 which initially accelerated ions of oxygen and sulphur at 200 GeV/nucleon. A subsequent upgrade of the ion injector in 1994 allowed to accelerate Pb ions up to an energy of 158 GeV/nucleon which were collided against fixed targets located in two experimental halls: one in the SPS north area (NA) and the other in the SPS west area (WA). Several fixed target experiments were built at the SPS between 1986 and 2005. After years of analyzing the Pb-Pb and Pb-Au fixed target collision data from SPS, CERN announced in 2000 that the combined results of the experiments NA44, NA45, NA49, NA50, NA52, WA97/NA57 and WA98, provided a first evidence of the creation of a new state of matter consistent with the QGP [39].

In the meantime, the first nucleus-nucleus collider known as the Relativistic Heavy Ion Collider (RHIC) started operations at the BNL in 2000. Two beams of Au are pre-accelerated at the AGS to an energy of 8.86 GeV/nucleon and then sent to RHIC where the Au beams are collided at $\sqrt{s_{NN}} = 130$ GeV. Other collision systems explored at RHIC include: p-p, p-Al, p-Au, d-Au, h-Au, Cu-Cu, Cu-Au and U-U. There are four detectors at RHIC called BRAHMS, PHENIX, STAR, and PHOBOS. Currently, only the STAR and PHENIX detectors are still active, while PHOBOS ceased operations in 2005 and BRAHMS in 2006. After four years of meticulously studying the system produced in Au-Au collisions with the four detectors, RHIC finally announced in 2005 the discovery of a strongly coupled QGP. Contrary to the expected gaseous behaviour, the QGP observed at RHIC turned out to resemble more a liquid with very little viscosity [40].

Currently, the largest heavy-ion collider is the Large Hadron Collider (LHC) at CERN

built in 2008. The SPS is used as injector to the LHC accelerating the Pb beams to energies of 1.38 TeV. The first nucleus-nucleus collisions at LHC took place in 2010 using Pb beams at 2.76 TeV. Since then, the LHC has collided different configurations involving ions, including p-Pb at 2.76 TeV (2013), Pb-Pb at 5.02 TeV (2015), p-Pb at 8.16 TeV (2016), Xe-Xe at 5.44 TeV (2017), and at the end of 2018 LHC is planning to provide a larger set of Pb-Pb collisions at 5.02 TeV. There are four detectors at the LHC called ALICE, CMS, ATLAS and LHCb. The four experiments are nowadays participating in the heavy-ion programme at LHC. Due to the large beam energies, the LHC is an ideal collider to study the QGP at very high temperatures, where one expects smaller QGP formation times and larger hot medium densities, compared to RHIC.

1.2.2 Geometry of nucleus-nucleus collisions

The number of particles produced in a nucleus-nucleus collision depends on the geometry of the collision. Since nuclei are extended objects made of nucleons (i.e. protons and neutrons), the number of nucleon-nucleon (NN) interactions increases the more head-on or central is the collision. The nucleons that participate in the collision are called participants while those that do not participate are called spectators. The overlap region of the collision is parameterized by the impact parameter \vec{b} which is the transverse distance between the centers of the two colliding nuclei as shown in Fig. 1.9.

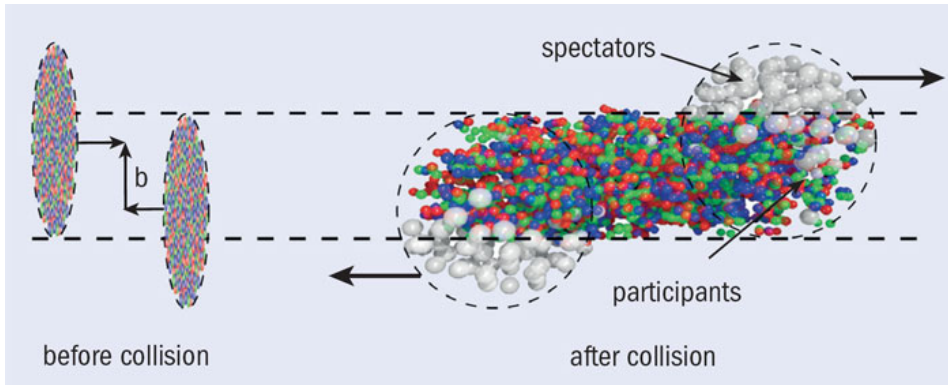


Figure 1.9: Illustration of two nucleus with impact parameter b before (left) and after (right) colliding. Figure taken from Ref. [31]

The formation of the QGP in nucleus-nucleus collisions depends on the number of colliding nucleons. To study the dynamics of the nuclear medium, the heavy-ion collisions are classified based on their centrality. The centrality c is defined as the fraction of the

total nucleus-nucleus inelastic cross section σ_{AB}^{inel} determined within the area defined by the impact parameter b , and it is expressed as $c = \pi b^2 / \sigma_{AB}^{inel}$.

The collision centrality can be related to the number of participants N_{part} and the number of binary NN collisions N_{coll} using a Glauber model. The Glauber model, developed in the 1950s by Roy Glauber, describes the collision between two nuclei as a superposition of NN interactions [41].

There are two ways of implementing the Glauber model, the optical and the Monte Carlo approach. In the optical approach, the physical observables are computed using the optical limit which assumes a continuous nucleon density distribution. On the other hand, in the Monte Carlo approach, the two nuclei are simulated by distributing the nucleons according to their nuclear density profile, and then the nucleus-nucleus collisions are modelled, at random impact parameters, by computing the individual NN collisions [41].

An example of a heavy-ion collision described by the optical Glauber model geometry is shown in Fig. 1.10. It represents the collision between a nucleus A with A nucleons and a nucleus B with B nucleons.

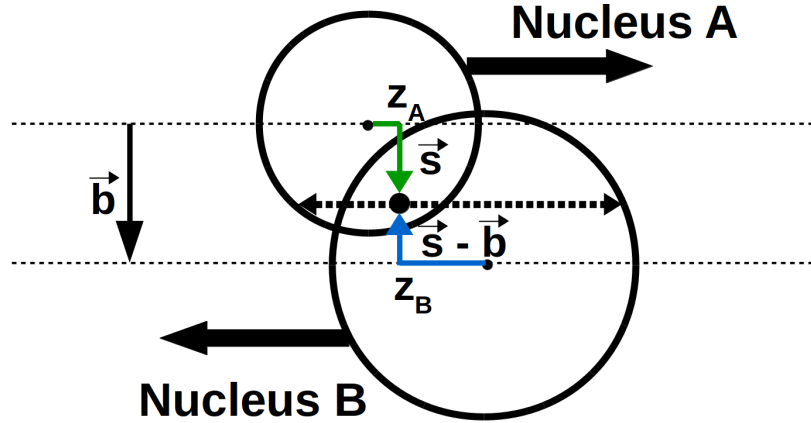


Figure 1.10: Schematic representation of the optical Glauber model geometry.

The tube located at a distance \vec{s} from the center of the nucleus A overlaps the tube located at a distance $\vec{b} - \vec{s}$ from the center of the nucleus B. In this case, the nuclear overlap function $T_{AB}(b)$ is defined as:

$$T_{AB}(b) = \int d^2s T_A(\vec{s}) T_B(\vec{b} - \vec{s}) \quad (1.9)$$

where T_A and T_B are the nuclear thickness functions of the nucleus A and B, respectively.

The nuclear thickness function is given by $T(\vec{r}) = \int \rho(\vec{r}, z) dz$, where ρ is the nuclear density distribution of a given nucleus which is generally parameterized with a Wood-Saxon density profile:

$$\rho(r) = \rho_0 \frac{1 + w(r/r_0)}{1 + \exp\left(\frac{r-r_0}{a}\right)} \quad (1.10)$$

where r is the distance to the center of the nucleus, a represents the width of the edge region of the nucleus called the skin depth, w measures the deviation from a spherical shape, and ρ_0 is a normalization factor such that the integral of the density is equal to the number of nucleons in the nucleus. Once the profile of the nucleus is parameterized, the average number of binary NN collisions $\langle N_{coll} \rangle$ for a given impact parameter b is defined as:

$$\langle N_{coll}(b) \rangle = AB T_{AB}(b) \sigma_{nn}^{inel} \quad (1.11)$$

where σ_{nn}^{inel} is the inelastic NN cross section. Hence, the Glauber model provides a quantitative description of the geometry of the nuclear collision and can be used to estimate the variables (N_{part} , N_{coll} and T_{AB}) for a given centrality class.

Experimentally, the impact parameter of the collision can not be determined directly. However, the distribution of the number of soft particles scales with N_{part} while the number of particles with large momentum transfer scales with N_{coll} . As a result, one can estimate the centrality by fitting the distribution of charged particles produced in the collision using the functions of N_{part} and N_{coll} derived from the Glauber model. In addition, the collision centrality can be inferred from the number of spectators determined from the measurement of the transverse energy in the forward region.

1.2.3 Evolution of heavy-ion collisions

The evolution of a nucleus-nucleus collision undergoes several steps, starting from the collision of the nuclei to the final production of hadrons. Fig. 1.11 illustrates the different processes that occur during a heavy-ion collision associated to the production of the QGP.

1. Initial stage: At very high energies, the two nuclei are Lorentz contracted along the axis of motion while approaching each other at almost the speed of light. As a consequence, the nucleons of each nuclei are also contracted increasing the number of gluons until it reaches the gluon saturation scale. The dynamics of the nucleus can be described using the Glauber model or by an effective theory called the Color

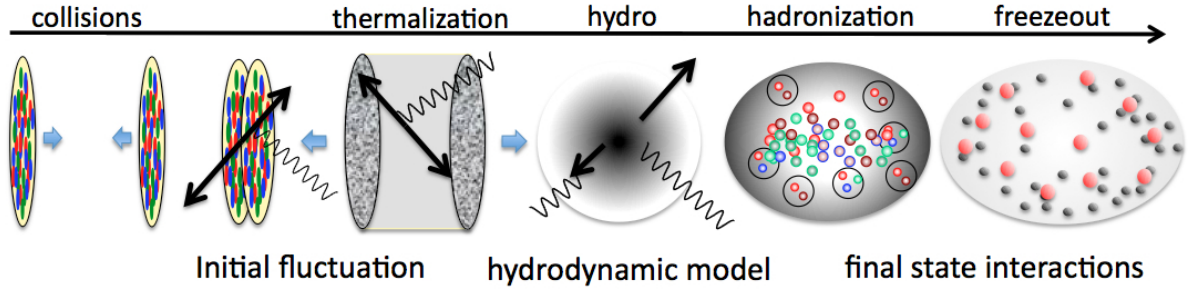


Figure 1.11: Schematic sketch of the evolution of a relativistic heavy ion collision. The wavy lines represent photons while the arrows correspond to jets. Figure taken from Ref. [31]

Glass Condensate (CGC). In addition, when the two nuclei collide, the partons inside the geometrical overlap region of the two nuclei undergo parton-parton interactions with large momentum transfers.

2. **QGP formation and thermalization:** The parton-parton interactions quickly start producing new particles increasing the density of the system until a phase transition is reached forming the QGP. After some time, the system reaches thermal equilibrium.
3. **Hydrodynamical expansion:** After reaching the thermal equilibrium, the system evolves as a perfect fluid. It first expands longitudinally along the beam direction and then it expands in all directions until the QGP reaches the critical temperature.
4. **Hadronization:** The medium undergoes a phase transition into a hadronic gas where the partons recombine into hadrons. In this phase, the system keeps expanding via hadron-hadron interactions until the average path length of the hadrons is as large as the size of the system.
5. **Freeze-out:** The hadron gas experience first a chemical freeze-out when the inelastic collisions between hadrons cease, fixing the composition of the particles. Subsequently, the system reaches the kinetic freeze-out when the elastic scattering

between the hadrons also stop, fixing the kinematic distributions of the particles. Subsequently, the particles escape the medium and are reconstructed in the detector.

1.2.4 Experimental probes of the QGP

The QGP can not be directly measured experimentally, since once it is created it only exists for a very short amount of time. Nonetheless, the QGP can be studied indirectly by measuring how the particles and the system produced in the collision is modified by the presence of the QGP. There are many experimental signatures that has been used to asses the different properties of the QGP, such as the enhancement of the strange quark production, suppression of the quarkonia yields, attenuation of the energy of jets, anisotropies in the azymuthal distribution of particles, among others. The production mechanism of each experimental probe depends on the momentum scale of the process. Signatures produced in processes involving large momentum transfer are called hard probes while those produced at low momemtum scales are called soft probes.

The majority of the particles produced in heavy-ions collisions are soft and constitute the bulk of the system. Soft probes are used to study the thermal and hydrodynamical evolution of the medium. The production yields of soft particles scales with the number of nucleons that participate in the collision. The strange hadron yields and the elliptic flow are two examples of soft probes. On the other hand, hard probes are produced from the parton-parton hard scattering during the initial stage of the collision. Hard probes are ideal tools to study the structure of the system produced in the collision since they live through the full evolution of the medium, and their production cross section can be factorized into a partonic cross section described by pQCD and the nPDFs of the nuclei (see Eq. (1.6)). The number of hard particles produced in the medium scales with the number of binary NN collisions. Some important hard probes used to study the nuclear medium includes the electroweak bosons, quarkonium and jets. The following subsections present a brief description on some of the soft and hard probes of the QGP.

1.2.4.1 Elliptic flow

When the QGP is formed, it undergoes a collective expansion due to the large pressure gradient produced by the multiple partonic interactions during the heavy-ion collision. This collective expasion is known as flow. The magnitude of the flow tend to grow with the number of parton-parton interactions and it depends on the initial conditions of the

collision. If the nucleus-nucleus collision is completely central ($b = 0$) then the particles develop a radial flow, but if the collision is non-central ($b \neq 0$) then the spatial anisotropy of the overlap region leads to an anisotropic flow as shown in Fig. 1.12.

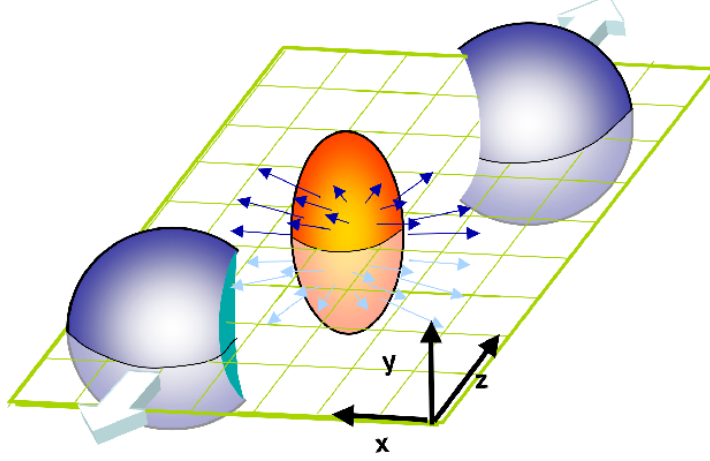


Figure 1.12: Sketch of the deformed medium and the elliptic flow produced in non-central heavy-ion collisions. Figure taken from Ref. [42]

Experimentally, the anisotropic flow can be determined from the Fourier decomposition of the particle azimuthal distribution with respect to the reaction plane ψ_{RP} [43]:

$$\frac{d^3N}{d^3\vec{p}} = \frac{1}{2\pi} \frac{d^2N}{p_T dp_T dy} \left(1 + 2 \sum_{n=1}^{\infty} v_n \cos[n(\phi - \psi_{RP})] \right) \quad (1.12)$$

where the Fourier coefficient v_2 measures the strength of the elliptic flow and the reaction plane is derived from the direction of the beam (z -axis) and the impact parameter (x -axis) as presented in Fig. 1.12.

An alternative way to derive the flow coefficients is by computing the Fourier decomposition of the two-particle azimuthal distribution defined as [43]:

$$v_n\{2\}^2 = c_n\{2\} = \langle \cos[n(\phi_1 - \phi_2)] \rangle \quad (1.13)$$

where $c_n\{2\}$ is called the two-particle cumulant and the brackets represent the average over all particles and events. The advantage of using particle correlations is that the Fourier coefficients do not depend on the reaction plane, but non-flow contributions (e.g. resonance decays) can affect the measurements. Higher orders of particle correlations, such as four-particle correlations, can reduce the impact of the non-flow effects.

The elliptic flow of the medium is sensitive to the equation of states of the QGP [43] and the bulk viscosity [44]. Furthermore, relativistic hydrodynamic calculations [45] predicts that the elliptic flow of hadrons can approximately be expressed as $v_2 \propto (p_T - \beta m_T)$, where β is the average flow velocity and m_T is the transverse mass of the hadron. As a consequence, the elliptic flow is expected to show a mass ordering where the more massive hadrons would have lower v_2 values compared to the lighter hadrons.

The low p_T -dependence of the elliptic flow of strange hadrons measured at RHIC in Au-Au collisions at $\sqrt{s_{NN}} = 200$ GeV is presented in Fig. 1.13. The measurement of the elliptic flow of π^\pm mesons, K_s^0 mesons, antiprotons and Λ baryons (with masses of 140, 495, 940 and 1,115 MeV, respectively), shows the expected mass ordering pattern as a function of the hadron p_T . Moreover, the good agreement between the RHIC results and the predictions using relativistic hydrodynamics assuming non-viscous flow supported the conclusion that the QGP behaves as an ideal fluid.

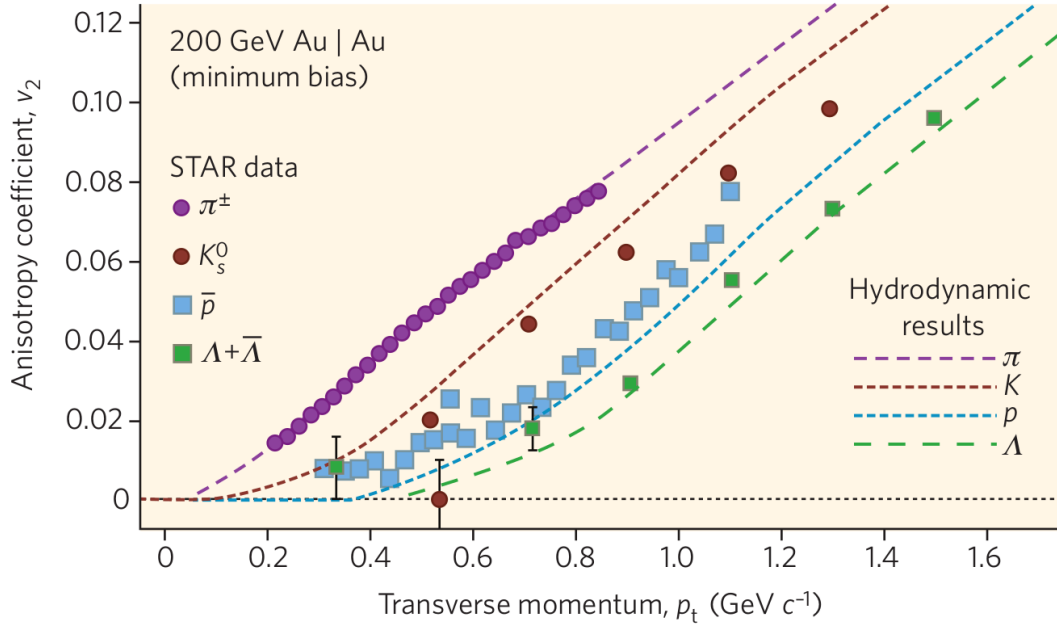


Figure 1.13: Elliptic flow distribution of as a function of transverse momentum for π^\pm mesons, K_s^0 mesons, antiprotons and Λ baryons measured by STAR collaboration in Au-Au collisions at $\sqrt{s_{NN}} = 200$ GeV. The results are compared with relativistic hydrodynamic calculations. Figure taken from Ref. [46]

1.2.4.2 Strangeness enhancement

Strange quarks belongs to the second generation of quarks and are roughly 20 (40) times more massive than the down (up) quarks. The number of strange quarks involved in a decay can be quantified through the quantum number called strangeness which can take values of +1, -1 and 0, for strange quarks, strange anti-quarks, and the other quarks, respectively. Strangeness is conserved in strong and electromagnetic interactions, while it is not conserved in weak decays. In hadronic collisions, strange quark-antiquark pairs ($s\bar{s}$) are produced in parton-parton interactions via gluon fusion ($gg \rightarrow s\bar{s}$) or quark annihilation ($q\bar{q} \rightarrow s\bar{s}$), and through gluon splitting ($g \rightarrow s\bar{s}$) during the evolution of the medium. The production of strange hadrons in proton-proton collisions is suppressed relative to hadrons made of light quarks (i.e. pions), due to the higher mass of the strange quark.

In heavy-ion collisions, where the QGP is formed, it was proposed by Johann Rafelski and Rolf Hagedorn [47] in 1980 that the enhancement of strangeness could serve as a signature of the QGP. Due to the large gluon density present in the hot medium, the gluon fusion becomes the dominant production mode of strange quark pairs in the QGP as shown in Fig. 1.14. When the temperature of the QGP decreases and the partons hadronize, the production of hadrons containing multi-strange (anti-)quarks is enhanced relative to the production of pions. Moreover, at high collision energies, the strange quarks can also bind to charm and bottom quarks during hadronization, producing many exotic hadrons (e.g. strange D_s or B_s mesons) that would otherwise be rarely seen without the presence of the QGP. As a consequence, one would expect an overall increase of strange quark pair production compared to pions, and also an enhancement of the production of multi-strange (anti-)hadrons in central heavy-ion collisions compared to proton-proton collisions [48]. The strangeness enhancement in the QGP can be described using a thermal model based on a grand canonical ensemble approach [49].

The enhancement of strange hadrons has been observed in SPS and RHIC [51]. Both experiments measured an increasing enhancement of the strangeness content of the hadrons. The ratios of the production yields at mid-rapidity of K^+/π^+ and Λ/π^- mesons for central nucleus-nucleus collisions, shown in Fig. 1.15, reach a maximum relative strangeness enhancement at $\sqrt{s_{NN}} \approx 8$ GeV, which has been interpreted as the energy during the transition to the QGP [51].

Recently, the ALICE collaboration published in [53] the observation of enhanced production of multi-strange hadrons in proton-proton collisions at $\sqrt{s} = 7$ TeV with high charged-particle multiplicities. The results at LHC show that the enhancement

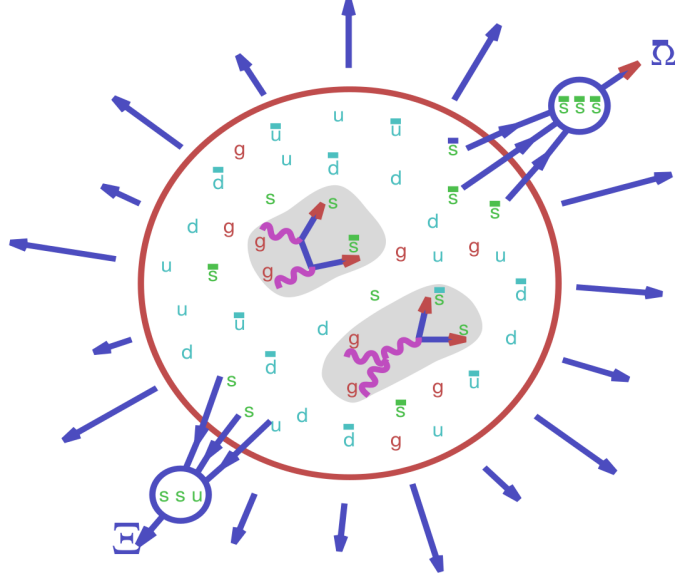


Figure 1.14: Sketch of the production of strange hadrons via gluon fusion in the QGP. Figure taken from Ref. [50]

of the strangeness production increases as a function of charged-particle multiplicity from high-multiplicity p-p to p-Pb to Pb-Pb collisions. Therefore, further studies of the mechanism of strangeness production at high multiplicities are necessary to understand the evolution of small systems.

1.2.4.3 Jet quenching

Energetic partons are produced in the hard scattering at the beginning of the collision. The scattered partons fragments into other colour charged particles which then creates an ensemble of hadrons during the hadronization process. The baryons and mesons produced at the end of the collision tend to move along the same direction as the original fragmented parton, forming a localized spray of particles called jet. The jets can be reconstructed by clustering hadrons and other particles around a cone using a jet sequential recombination algorithm (e.g. anti- k_t [54]).

In heavy-ion collisions, the hard partons lose energy when they traverse the hot medium either by multiple scattering with the medium constituents or by medium-induced gluon radiation, been the later the dominant mode of parton energy loss in the QGP. As a consequence, the energy of the jets is attenuated and the jets are considered quenched by the medium. The phenomenon of jet quenching in the QGP was first

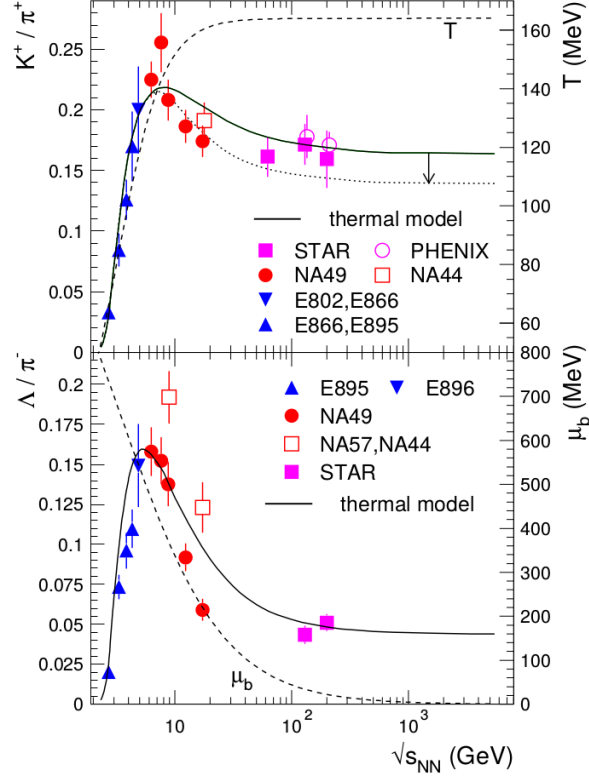


Figure 1.15: Energy distribution of the relative production ratios K^+/π^+ and Λ/π^- at mid-rapidity measured at AGS (E802, E866, E895, E896) and SPS (NA44, NA49, NA57) in central Pb-Pb collisions, and at RHIC (STAR, PHENIX) in central Au-Au collisions. The solid line is the result of a statistical model calculation. The dotted line shows the K^+/π^+ ratio including the additional effect of higher mass resonances. The dashed lines show the energy dependence of the temperature (upper panel) and baryonic density (lower panel). Figure taken from Ref. [52]

proposed in 1982 by James Bjorken. Bjorken suggested in [55] that the observation of events with two jets, where one of the jets escape the QGP without losing energy while the other jet is fully quenched as shown in Fig. 1.16, could be used as a probe to determine the presence of the QGP.

The first direct observation of jet quenching was determined at the LHC after measuring an enhanced dijet asymmetry in Pb-Pb collisions compared to proton-proton collisions. The dijet asymmetry is quantified by measuring the jet energy imbalance between the two highest transverse energy jets with an azimuthal angle separation of $\Delta\phi = |\phi_1 - \phi_2| > \pi/2$. The jet energy imbalance A_J is derived as:

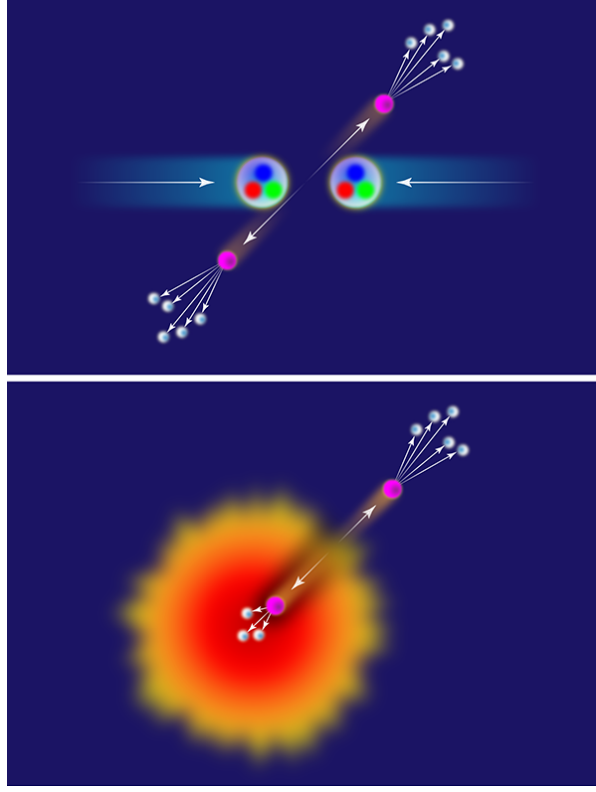


Figure 1.16: Sketch of the production mechanism of two jets in proton-proton (top) and heavy-ions (bottom) collisions. Figure taken from Ref. [56]

$$A_J = \frac{E_{T1} - E_{T2}}{E_{T1} + E_{T2}} \quad (1.14)$$

where E_{T1} is the transverse energy of the most energetic jet among the pair of jets. Fig. 1.17 presents the results, published by the ATLAS collaboration, of the dijet asymmetry distribution and the azimuthal angle between the two jets in different bins of centrality. The dijet asymmetry measured in Pb-Pb collisions at $\sqrt{s_{NN}} = 2.76$ TeV are compared to the measurements from p-p collisions at $\sqrt{s} = 7$ TeV and the simulated results derived using events from the Heavy Ion Jet Interaction Generator (HIJING) superimposed with PYTHIA events. The LHC results show a significant dijet energy imbalance in Pb-Pb collisions which increases with the centrality of the collision. This dijet asymmetry is not seen in p-p collisions evidencing the strong jet energy loss present in the QGP.

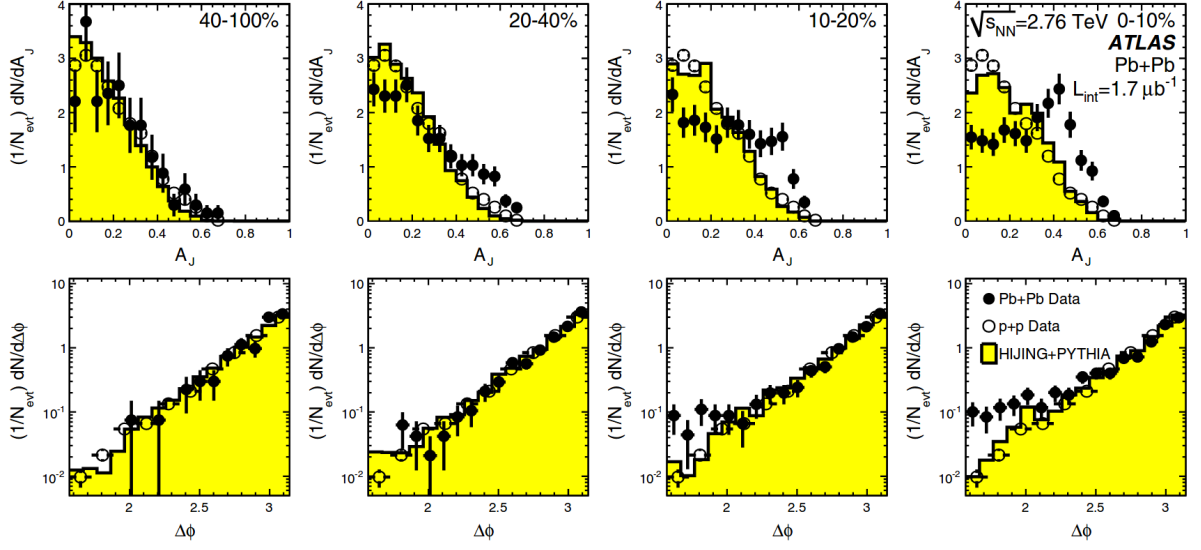


Figure 1.17: Dijet asymmetry measured by the ATLAS collaboration in lead-lead collisions at $\sqrt{s_{NN}} = 2.76$ TeV (points) and proton-proton collisions at $\sqrt{s} = 7$ TeV (open circles). The top panel shows the dijet asymmetry distributions and unquenched HIJING with superimposed PYTHIA dijets (solid yellow histograms), as a function of collision centrality. The bottom panel shows the distribution of the azimuthal angle between the two jets $\Delta\phi$, for data and HIJING+PYTHIA, also as a function of centrality. Figure taken from Ref. [57]

1.2.4.4 Quarkonium production

Quarkonium ($Q\bar{Q}$) is a meson composed of a heavy quark and its own anti-quark. Quarkonium can be classified as charmonium or bottomonium if it is made of charm quarks or bottom quarks, respectively. The ground state of charmonium is called J/ψ meson while the one for bottomonium is called $\Upsilon(1S)$ meson. The properties of quarkonia are non-perturbative but since the mass of the heavy quarks is comparable to the mass of the quarkonia, the quarks move inside the quarkonia much slower than the speed of light. As a result, the properties of quarkonia can be computed using an effective non-relativistic model. For instance, one way to describe the binding of the quarks is by using a Cornell potential [58] given by:

$$V_{Q\bar{Q}}(r) = -\frac{a}{r} + br \quad (1.15)$$

where r is the binding radius of the quarkonium, a is the coulombic interaction coupling, and b is the string tension. The binding radius increases for higher excited

states of charmonium (e.g. $\psi(2S)$) and bottomonium (e.g. $\Upsilon(2S)$ and $\Upsilon(3S)$) compared to their corresponding ground states (i.e. $r_{\Upsilon(1S)} < r_{\Upsilon(2S)} < r_{\Upsilon(3S)}$).

One of the first signatures suggested to probe the QGP was the suppression of J/ψ meson production. In 1986, Tetsuo Matsui and Helmut Satz [59] proposed that the J/ψ meson binding potential gets screened in the QGP due to the interactions with the free colour charged constituents of the hot medium. The Debye colour screening potential increases with the temperature of the medium until the binding potential can no longer hold the quarks together, and the quarkonium "melts". The binding potential of quarkonium states gets weaker for larger binding radius. As a result, the higher excited states of quarkonium are expected to be more dissociated at a given temperature compared to the ground state, leading to a sequential suppression of quarkonia.

The sequential suppression of bottomonia states has been observed at the LHC. Fig. 1.18 shows the invariant mass distribution of dimuons measured by the CMS collaboration in Pb-Pb collisions at $\sqrt{s_{NN}} = 5.02$ TeV. The result is compared to the invariant mass distribution obtained by adding the bottomonium mass peaks extracted from p-p collisions at $\sqrt{s} = 5.02$ TeV on top of the Pb-Pb background and normalized to the $\Upsilon(1S)$ mass peak in Pb-Pb. The comparison shows a clear suppression pattern where the $\Upsilon(3S)$ is completely melted while part of the $\Upsilon(2S)$ mass peak still survives.

The first evidence of J/ψ meson suppression was observed in Pb-Pb collisions at 158 GeV/nucleon by the NA50 collaboration at SPS [61]. The results at SPS showed that the J/ψ meson cross section measured in peripheral collisions was consistent with the expectations from nuclear absorption while in central collisions it was more suppressed [62]. However, the measurement of the J/ψ meson production in Au-Au collisions at $\sqrt{s_{NN}} = 200$ GeV at RHIC showed a similar level of suppression compared to SPS, contrary to the higher expected suppression due to the higher beam energies.

To understand the measurements of J/ψ meson production at SPS and RHIC, it was proposed that the J/ψ meson production could also be enhanced at RHIC energies. According to [?], the J/ψ mesons could be regenerated in the most central collisions from the statistical hadronization of uncorrelated charm quark pairs produced in the hard scattering. The number of directly produced $c\bar{c}$ pairs in central nucleus-nucleus collisions is expected to be small at SPS energies, but it can reach values of more than 10 and 100 charm quark pairs at RHIC and LHC energies, respectively [63]. The statistically regenerated J/ψ mesons are mainly produced at low p_T since the directly produced charm quarks reach thermal equilibrium before hadronizing [?].

In order to quantify how the hot nuclear medium modifies the production of quarkonia,

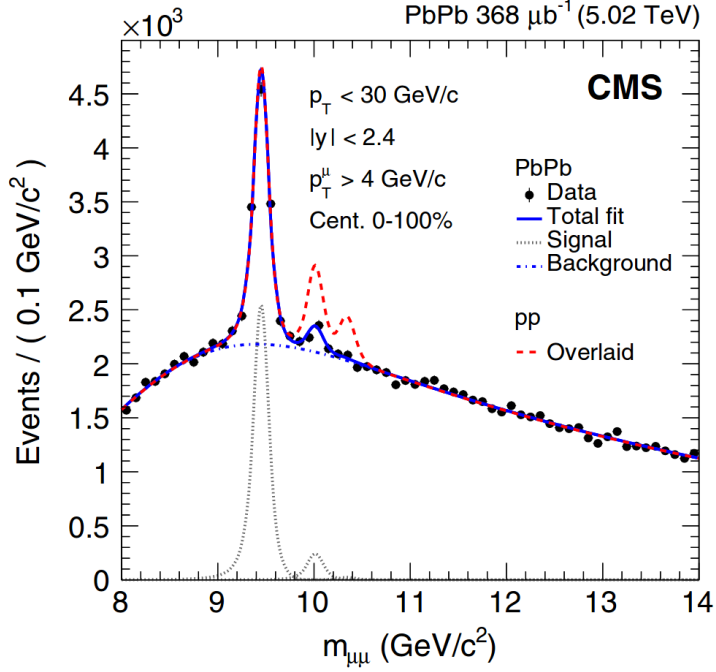


Figure 1.18: Dimuon invariant mass distribution measured by the CMS collaboration in Pb-Pb collisions at $\sqrt{s_{NN}} = 5.02$ TeV. The total fit (solid blue line), the background component (dot-dashed blue line) and the individual $\Upsilon(1S)$, $\Upsilon(2S)$ and $\Upsilon(3S)$ mass peaks (dotted gray lines) are shown. The dashed red line represents the p-p signal shapes added on top of the Pb-Pb background and normalized to the $\Upsilon(1S)$ mass peak in Pb-Pb. Figure taken from Ref. [60]

one can measure the nuclear modification factor R_{AA} defined as:

$$R_{AA} = \frac{N^{AA}}{\langle N_{coll} \rangle N^{pp}} \quad (1.16)$$

where N^{AA} is the yield of particles measured in nucleus-nucleus collisions, N^{pp} is the same yield measured in proton-proton collisions, and $\langle N_{coll} \rangle$ is the average number of binary nucleon-nucleon collisions. Proton-proton collisions are used as a reference since the average energy density of the medium is not enough to produce the QGP.

The measurements of the J/ψ meson production has also been performed at the LHC. The results of the J/ψ meson nuclear modification factor measured by the ALICE collaboration in the 0% – 20% most central Pb-Pb collisions at $\sqrt{s_{NN}} = 2.76$ TeV are compared in Fig. 1.19 to the results measured by the PHENIX collaboration in the 0% – 20% most central Au-Au collisions at $\sqrt{s_{NN}} = 200$ GeV. The J/ψ R_{AA} measured at the LHC is larger than the one measured at RHIC at low J/ψ meson p_T , consistent with

the trend predicted by the statistical regeneration model of charmonia.

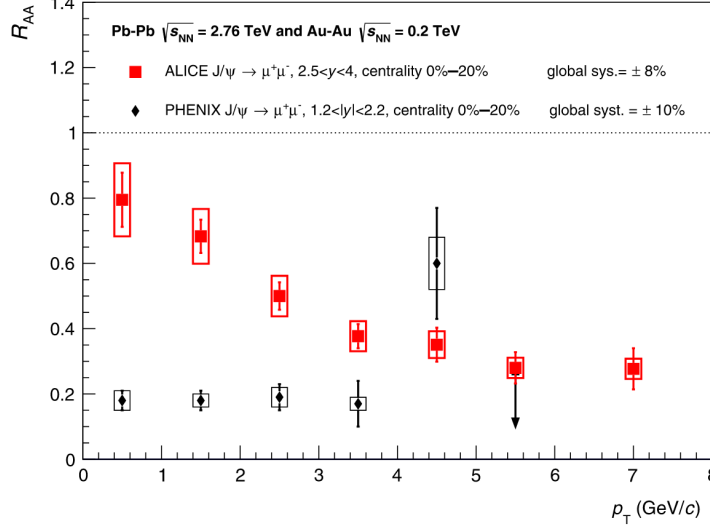


Figure 1.19: Nuclear modification factor of J/ψ meson as a function of transverse momentum measured by the ALICE collaboration in the 0% – 20% most central Pb-Pb collisions at $\sqrt{s_{NN}} = 2.76$ TeV compared to results from the PHENIX collaboration measured in the 0% – 20% most central Au-Au collisions at $\sqrt{s_{NN}} = 200$ GeV. Figure taken from Ref. [64]

1.2.4.5 Electroweak boson production

Electroweak particles, such as W bosons and Z bosons, are produced in the parton-parton hard scattering and they do not interact strongly with the nuclear medium produced in the heavy-ion collisions. As a result, electroweak bosons are good probes of the initial stage of the proton-nucleus (p-A) and nucleus-nucleus (A-A) collisions. The dominant production mode of electroweak bosons in heavy-ion collisions is via the annihilation of a light quark and anti-quark. The large momentum scales involved in the production of weak bosons allows to derive precise calculations of their partonic cross sections using pQCD.

The production yields of electroweak bosons in proton-nucleus collisions are affected by the mix of protons and neutrons in the colliding nucleus (isospin effect), and the depletion (shadowing) or enhancement (antishadowing) of the PDFs in the nucleus. Thus, the measurement of the electroweak boson production in p-A can be used to set constraints to the global fits of the nuclear PDFs. In nucleus-nucleus collisions, the measurement of the nuclear modification factor of Z bosons at the LHC in Pb-Pb collisions

at $\sqrt{s_{NN}} = 2.56$ TeV, presented in Fig. 1.20, shows that the production of weak bosons is not modified by the hot nuclear medium and only scales with N_{coll} , which could be used as an indirect way to determine the centrality of the collision.

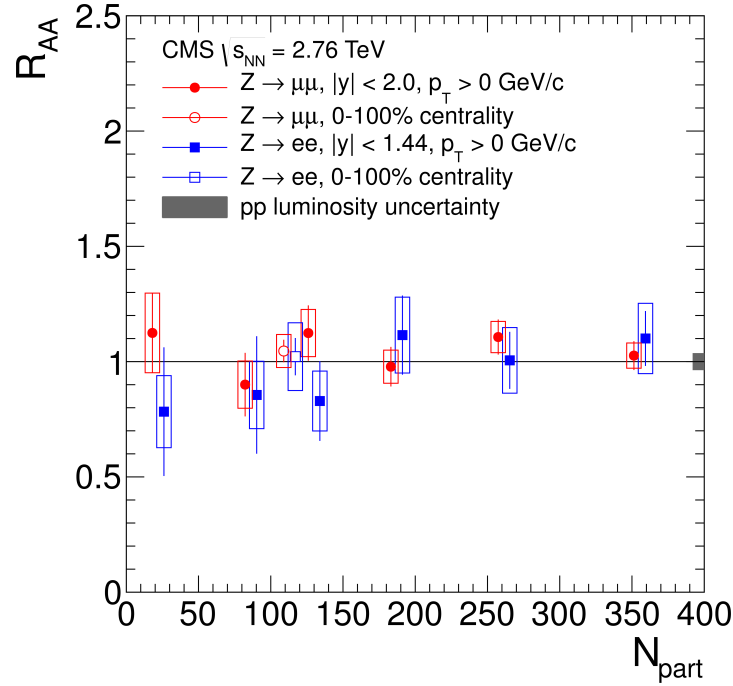


Figure 1.20: Nuclear modification factor R_{AA} of $Z \rightarrow e^+e^-$ (blue squares) and $Z \rightarrow \mu^+\mu^-$ (red circles) events as a function of the number of participants measured by the CMS collaboration in Pb-Pb collisions at $\sqrt{s_{NN}} = 2.56$ TeV. The open points represent the centrality-integrated R_{AA} and the vertical lines (boxes) correspond to statistical (systematic) uncertainties. The grey bar at $R_{AA} = 1$ represents the uncertainty of the luminosity determined in proton-proton collisions. Figure taken from Ref. [65]

EXPERIMENTAL SETUP

This chapter
BlaBla

2.1 Experimental setup

2.1.1 Large Hadron Collider

2.1.2 CMS detector

2.1.3 Trigger System

2.1.4 Object reconstruction

This chapter
BlaBla

3.1 Theory

3.2 Analysis

3.3 Results

W BOSON PRODUCTION IN PROTON-LEAD COLLISIONS

This chapter describes the measurement of the production of W bosons in proton-lead (pPb) collisions at a nucleon-nucleon center-of-mass energy $\sqrt{s_{\text{NN}}} = 8.16$ TeV with the CMS detector. As mentioned in Section ??, the primary processes that contribute at LHC energies to the production of W bosons are $u\bar{d} \rightarrow W^+$ and $d\bar{u} \rightarrow W^-$. Once produced, W bosons can decay weakly to either leptons or quarks. The semi-muonic decay ($W \rightarrow \mu\nu_\mu$) is of particular interest, since muons lose negligible energy in the medium and the surrounding background is small.

The individual W^+ and W^- production rates are expected to be modified relative to proton-proton (pp) collisions, due to the different content of up and down quarks in the proton compared to the lead nuclei. The distribution of partons inside the nuclei can also be modified by parton shadowing (or depletion), which can alter the W boson yields at the LHC. Precise measurements of W production in pPb collisions can therefore provide strong constraints to the nuclear parton distribution functions (nPDF).

The analysis is currently being reviewed. Previous results have been published by the CMS collaboration on pPb data at $\sqrt{s_{\text{NN}}} = 5.02$ TeV collected in 2013 [66]. A similar study has been performed by the ALICE [67] and the ATLAS [68] collaborations at pPb collision energies of 5.02 TeV.

The datasets and simulated samples are described in Section ?. In Section ?, the event selection is presented. The relevant backgrounds are introduced in Section ?. Finally, the systematic uncertainties are discussed in Section ? and the results are

24 detailed in Section 4.2.

25 4.1 Theory

26 4.1.1 History of weak theory

27 In the early 20th century, quantum mechanics was the standard framework of atomic
 28 physics but certain processes such as the β decay, discovered by Ernest Rutherford in
 29 1899 [69], were not fully understood yet. At the time, the β decay was characterized
 30 by the process $A_i \rightarrow A_f + e^-$, where an initial nucleus A_i decays into another nucleus
 31 A_f emitting an electron during the process. In order to conserve energy, the electron
 32 is required to have a fixed kinetic energy, but James Chadwick observed in 1914 that
 33 the β rays produced a continuous energy spectrum [70, 71] in disagreement with was
 34 expected. As a way to solve the problem of the continuous β decay spectrum, Wolfgang
 35 Pauli proposed in 1930 the existence of a new particle [72, 73]. Pauli named his particle
 36 initially the neutron but later renamed it to the neutrino after the discovery of a new
 37 electrically neutral particle inside the ${}^{14}_7\text{Ni}$ nucleus by Chadwick in 1932 [74]. Pauli
 38 described the neutrino as a neutral fermion with mass close to zero and spin 1/2 capable
 39 of penetrating matter deeper than photons [72].

40 Enrico Fermi, after attending the 7th Solvay conference where the discovery of the
 41 neutron as well as Pauli's neutrino were presented, proposed a new theory to explain
 42 the β decay [75]. Fermi's theory defined the β decay as a process in which the neutron
 43 decays to a proton, emitting an electron and a neutrino. Fermi formulated his theory
 44 using an analogous approach as in Quantum Electrodynamics (QED) by proposing the
 45 following lagrangian for β decay [76]:

$$L_\beta = G_F (\bar{u}_p \gamma_\mu u_n) (\bar{u}_e \gamma^\mu u_\nu) \quad (4.1)$$

46 where u is the Dirac spinor of each particle, γ_μ is the Dirac matrix and G_F is the Fermi
 47 coupling constant. Fermi's theory of weak interactions assumed the same conservation
 48 rules as QED, including the symmetry under reflection in space [76]. A system that is
 49 invariant under reflections conserve a quantity called parity which includes an intrinsic
 50 component called spin and a spatial component depending on the angular momentum of
 51 the particle.

52 In the upcoming years, the physicists Tsung Dao Lee and Chen Ning Yang started to
 53 doubt the conservation of weak parity after not finding any experimental evidence so

far [77]. In an attempt to test the conservation of parity in weak interactions, Lee and Yang proposed in 1956 to study the β decays of Cobalt (^{60}Co) and measure the projection of the momentum of electrons along the spin axis of the Cobalt nucleus [77]. If the decay process conserves parity then electrons would be produced in all directions. The experiment to test the conservation of weak parity was realized by Chien-Shiung Wu in 1957. The results of Wu's research showed that electrons were preferentially produced in the opposite direction to the Cobalt spin [78], which meant that parity was not conserved in weak interactions.

Apart from parity, one can also associate a helicity to particles. The particle's helicity is considered right-handed if the direction of the particle's momentum and spin are the same, and left-handed otherwise. In 1958, Goldhaber, Grodzins and Sunyar measured the neutrino helicity at Brookhaven National Laboratory (BNL) and discovered that neutrinos were always left-handed and antineutrinos were right-handed [79]. As a consequence of the discovery of parity violation and the neutrino helicity, Robert Marshak and George Sudarshan modified Fermi's weak theory and introduced an axial vector term, giving rise to the V-A (vector-axial) theory of weak interactions [80]. Even though parity (P) and charge conjugation (C) (transforms particles into their antiparticles) were violated separately, it was assumed that the combined CP operation was still conserved by the weak force.

The assumption of the conservation of CP did not last long. An experiment performed at BNL by James Christenson, James Cronin, Val Fitch and Rene Turlay [81] in 1964 concluded that the long-lived K_L meson ($\text{CP}=-1$) was able to decay to two pions ($\text{CP}=+1$) violating CP in the process. To explain the CP violation in weak theory, Makoto Kobayashi and Toshihide Maskawa [82] extended the formulation of the Cabibbo matrix to include three generation of quarks and a CP-violating phase term. The Cabibbo matrix was originally computed by Nicola Cabibbo [83] including four quarks to explain the different amplitudes observed between the up, down and strange quark transitions. The development of the Cabibbo, Kobayashi and Maskawa (CKM) matrix led to the prediction of the bottom and top quarks, discovered later in 1977 [84] and 1995 [85], respectively.

Following Paul Dirac's formulation of QED [86], Sheldon Glashow [87], Steven Weinberg [88] and Abdus Salam [89] managed in 1968 to build a gauge-invariant unified theory of the electromagnetic and weak interactions, for which they were awarded the Nobel Prize in Physics in 1979 [90]. In order to make the electroweak theory symmetric under local phase transformations, it required the presence of four spin-1 massless bosons: two electrically charged particles called W^\pm bosons and two neutral particles

89 corresponding to the Z boson and photon. But since weak interactions are short range,
90 the weak force has to be mediated by massive bosons. The addition of mass to the bosons
91 was realized after introducing the spontaneous local breaking of the underlying SU(2)
92 symmetry through the Higgs mechanism [8, 9]. In the following years, Gerardus't Hooft
93 and Martinus Veltman managed to renormalize the electroweak theory [91, 92], allowing
94 to calculate more precisely the theoretical masses of the weak bosons.

95 The experimental study of weak bosons would require the development of new
96 particle acceleration technologies. In 1976, Carlo Rubbia, Peter McIntyre and David
97 Cline suggested to transform CERN's circular proton accelerator called Super Proton
98 Synchrotron (SPS) into a proton-antiproton collider (Sp \bar{p} S) [93]. The upgrade to Sp \bar{p} S
99 was made possible thanks to the stochastic cooling technology invented by Simon Van
100 der Meer [94] in 1972, which allowed to cool down and collect antiprotons. Several
101 experiments, named Underground Area (UA), were built to study the proton-antiproton
102 collisions at the Sp \bar{p} S. The UA1 and UA2 collaborations discovered the W boson [95, 96]
103 in 1983 after reporting the observation of electrons with large transverse energy and
104 the presence of missing energy in $p\bar{p}$ collisions at $\sqrt{s} = 540$ GeV. And few months later,
105 both collaborations also reported the discovery of the Z boson in the dilepton decay
106 channel [97, 98]. These outstanding discoveries convinced the Swedish Academy of
107 Science to award in 1984 the Nobel Prize in Physics to Rubbia and Van der Meer for
108 their contributions to the Sp \bar{p} S program [99].

109 After the major success of the Sp \bar{p} S project, CERN constructed in 1983 a new lep-
110 ton circular collider called the Large Electron-Positron (LEP) collider [100]. LEP was
111 designed to accelerate electrons and positrons to an energy of half the Z boson mass
112 (45 GeV) in order to perform precision measurements of the Z boson lineshape. Fur-
113 thermore, a precise measurements of the W mass [101] was later performed by the
114 experiments in the Fermi National Accelerator Laboratory (FNAL). The FNAL analyzed
115 data collected between 1983 and 2011 from the Tevatron [102], a proton-antiproton
116 synchrotron collider that operated at energies up to 1 TeV.

117 The succesful programs of LEP and Tevatron produced the most precise measure-
118 ments of the properties of the electroweak theory, but there was still a missing piece
119 to complete the picture, the Higgs boson. The discovery of the Higgs boson was finally
120 achieved in 2012 by the CMS [10] and ATLAS [11] collaborations at the Large Hadron
121 Collider (LHC).

4.1.2 Electroweak theory

The interactions between elementary particles mediated by the weak and electromagnetic forces are described in the Standard Model using the electroweak theory developed by Glashow, Weinberg and Salam [87–89]. The unification of these two fundamental forces of nature is accomplished mathematically using a non-abelian $SU(2) \times U(1)_Y$ gauge theory. The electroweak theory requires four massless gauge bosons: three bosons with weak isospin (called W_1 , W_2 and W_3) from $SU(2)$ and one boson (named B) with weak hypercharge from $U(1)_Y$.

Since weak bosons have mass, a full description of the electroweak interactions requires the inclusion of massive vector bosons. The problem is that one can not naively add a mass term of the form $m^2 W^\mu W_\mu$ into the electroweak lagrangian since this would break gauge invariance making the theory divergent. Thus, this issue is instead solved by spontaneously breaking the $SU(2) \times U(1)_Y$ electroweak symmetry into a $U(1)_{EM}$ symmetry using the Higgs mechanism [8, 9]. The overall idea is that the electroweak gauge bosons couple to a scalar field called the Higgs field which is present in all space. When the Higgs field induces a spontaneous breaking of the gauge symmetry, the Higgs field is splitted into one dynamic part corresponding to the Higgs boson, and another constant part called the vacuum expectation value (VEV). The symmetry breaking of $SU(2) \times U(1)_Y$ to $U(1)_{em}$ generates three massless Goldstone bosons. The goldstone bosons are then absorbed by the electroweak gauge bosons producing the W^+ , W^- and Z bosons with masses proportional to the VEV, while the photon remains massless. The W^\pm , Z and γ bosons are correlated with the W_1, W_2, W_3 and B gauge bosons in the following way:

$$\begin{aligned}
 W^\pm &= \frac{1}{\sqrt{2}}(W_1 \pm W_2) \\
 \begin{pmatrix} Z \\ \gamma \end{pmatrix} &= \begin{pmatrix} \cos\theta_W & \sin\theta_W \\ -\sin\theta_W & \cos\theta_W \end{pmatrix} \begin{pmatrix} B \\ W_3 \end{pmatrix}
 \end{aligned} \tag{4.2}$$

where θ_W represents the weak mixing angle. In addition, the quarks acquire mass through the Yukawa interaction with the Higgs field. Since the quark weak eigenstates are not the same as their mass eigenstates, weak interactions can induce a transition from a up-like quark (u, c, t) to a down-like quark (d, s, b). The strength of the quark flavour mixing in weak decays is parameterized by the CKM matrix V_{CKM} via:

$$\begin{pmatrix} d' \\ s' \\ b' \end{pmatrix} = \begin{pmatrix} V_{ud} & V_{us} & V_{ub} \\ V_{cd} & V_{cs} & V_{cb} \\ V_{td} & V_{ts} & V_{tb} \end{pmatrix} \begin{pmatrix} d \\ s \\ b \end{pmatrix} \quad (4.3)$$

150 where (d', s', b') are the down-like quark weak eigenstates and (d, s, b) are the
151 corresponding mass eigenstates. The latest values of the CKM matrix elements are [12]:

$$V^{\text{CKM}} = \begin{pmatrix} 0.97417 & 0.2248 & 0.00409 \\ 0.220 & 0.995 & 0.0405 \\ 0.0082 & 0.04 & 1.009 \end{pmatrix} \quad (4.4)$$

152 The lagrangian of the electroweak theory includes several components that describes
153 the interactions between the fermions, electroweak bosons and the Higgs boson. In the
154 case of the Z boson, the term of the lagrangian that represents the interactions between
155 fermions and neutral charged electroweak bosons is:

$$L_{NC} = \alpha_{em} \theta_W \sum_{\text{fermions}} \bar{f} \gamma^\mu A_\mu f + \frac{g}{\cos \theta_W} \sum_{\text{fermions}} \bar{f} \gamma^\mu \frac{(g_v^f - g_a^f \gamma^5)}{2} Z_\mu f \quad (4.5)$$

156 where g is the coupling constant of $SU(2)_L$, f is the Dirac spinors of fermions, A_μ
157 is the electromagnetic field, and g_v^f (g_a^f) is the fermion vector (axial) weak coupling
158 constants. Eq. (4.5) specify that the Z bosons and photons conserve flavour always
159 decaying into a fermion and its corresponding antifermion. Even though photons do
160 not distinguish the helicity of particles, the Z boson couplings are different for left- and
161 right-handed fermions.

162 Furthermore, the component of the lagrangian that represents the interaction be-
163 tween the W bosons and the fermions is given by:

$$L_{CC} = \frac{g}{2\sqrt{2}} \left((\bar{u}, \bar{c}, \bar{t})_R W_\mu^+ \gamma^\mu V^{\text{CKM}} \begin{pmatrix} d_L \\ s_L \\ b_L \end{pmatrix} + (\bar{\nu}_e, \bar{\nu}_\mu, \bar{\nu}_\tau)_R W_\mu^+ \gamma^\mu \begin{pmatrix} e_L^- \\ \mu_L^- \\ \tau_L^- \end{pmatrix} \right) \quad (4.6)$$

164 where f_L correspond to left-handed fermions and \bar{f}_R represents right-handed an-
165 tifermsions. Thus, W bosons only couple to right-handed antifermions and left-handed
166 fermions organized in pairs of lepton-neutrino or quark-antiquark, where the electric
167 charge of the of particles differ by one unit. Since the top quark mass (178 GeV) is larger
168 than the W boson mass (80 GeV), the W boson can not decay to a top quark. Fig. 4.1

shows the possible decays of W bosons to fermions. The measured values of the mass, width and couplings of weak vector bosons are summarized in Table 4.1.2.

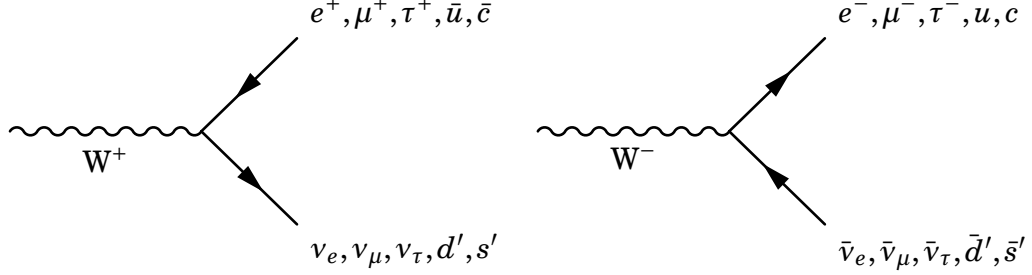


Figure 4.1: Feynman diagram of the decay modes of W^+ (left) and W^- (right) bosons to fermions.

Variable	Description	Value
M_W	W boson mass	80.385 ± 0.015 GeV
Γ_W	W boson width	2.085 ± 0.042 GeV
$\text{BR}(W \rightarrow \ell \nu)$	Branching fraction of W boson semileptonic decays	$(10.86 \pm 0.09)\%$
$\text{BR}(W \rightarrow q \bar{q}')$	Branching fraction of W boson hadronic decays	$(67.41 \pm 0.27)\%$
M_Z	Z boson mass	91.1876 ± 0.0021 GeV
Γ_Z	Z boson width	2.4952 ± 0.0023 GeV
$\text{BR}(Z \rightarrow \ell^+ \ell^-)$	Branching fraction of Z boson charged-lepton decays	$(3.3658 \pm 0.0023)\%$
$\text{BR}(Z \rightarrow \nu \bar{\nu})$	Branching fraction of Z boson neutrino decays	$(20.00 \pm 0.06)\%$
$\text{BR}(Z \rightarrow q \bar{q})$	Branching fraction of Z boson hadronic decays	$(69.91 \pm 0.06)\%$

Table 4.1: Experimental values of the mass, width and branching fractions of weak bosons extracted from the PDG [12].

4.1.3 Nuclear PDF

Beams of Pb ions composed of 82 protons and 126 neutrons are used at the LHC. In proton-lead collisions, the PDF of the nucleons (i.e. neutrons and protons) is modified by the presence of the nuclear environment of the Pb ion. The neutron PDF can be derived from the proton PDF using isospin symmetry (i.e. by exchanging the up and down quark PDFs), while assuming the same gluon PDF as in the proton. If no nuclear modifications are expected, protons and neutrons should then behave as free particles inside the nucleus, and one could simply sum the PDFs of the protons and neutrons scaled accordingly. In this case, the ratio of the PDF of protons bounded in the nucleus (nuclear PDF) over the free-proton PDF should be one.

181 To determine the nuclear modifications, the heavy ion measurements were first com-
 182 pared to results using deuterium. The European Muon Collaboration (EMC) measured
 183 the structure function of DIS in iron and deuterium targets between 1977 and 1988,
 184 and observed a depletion of the iron PDFs relative to the deuterium PDFs at $x > 0.2$
 185 (EMC region) [103] and at $x < 0.01$ (shadowing region) [104]. Subsequent results found
 186 an enhancement at the intermediate region $0.01 < x < 0.2$ (antishadowing region) [105].
 187 Since current heavy ion data is more limited than data from proton collisions, the global
 188 fits of the nuclear PDFs are less accurate than the proton PDFs.

189 4.1.4 PDF global fits

190 The parton distribution functions can not be currently determined from first principles
 191 due to the nonperturbative behaviour of the strong interactions. Nevertheless, their
 192 dependence on x can be derived by fitting observables (e.g. structure functions or asym-
 193 metries) to experimental data from different processes since PDFs do not depend on the
 194 initial hard scattering. The Q^2 dependence of the PDFs is determined using the DGLAP
 195 evolution equations. The most common processes used to constrain the PDFs correspond
 196 to Drell-Yan, DIS, vector boson and jet production, which have been measured by various
 197 experiments including data from HERA, SLAC and LHC.

198 There are several proton PDFs currently available. One of the most commonly used
 199 proton PDF in high energy physics nowadays is the one provided by the Collaboration
 200 of Theorists and Experimentalist (CTEQ). The most recent CTEQ PDF corresponds to
 201 CT14 published in 2016 [106]. The global fits of CT14 PDFs include data of vector bosons
 202 and jets from LHC pp collisions at 7 TeV and 8 TeV, charm quark DIS production from
 203 HERA, and electron charge asymmetry from Tevatron. The x -dependence of the CT14
 204 PDF is parameterized at low Q^2 scale by [106]:

$$xf_a(x, Q^2) = x^{c_1} (1-x)^{c_2} P_a(x) \quad (4.7)$$

205 where P_a is a polynomial with different parameters for each parton. In the case of
 206 the up and down valence quarks, P_a is expressed as a Bernstein polynomial of fourth-
 207 order in \sqrt{x} . The P_a distribution of gluon and the light sea quark PDFs is given instead
 208 by a Bernstein polynomial in $y = (2\sqrt{x} - x)$ of second-order and fourth-order, respectively.
 209 There is not enough data to constrain the strange quark and antiquark PDFs so they
 210 are assumed to be equal. In total, the CT14 PDFs are described by 26 fitting parameters

including: 8 parameters for the valence quarks, 5 parameters for the gluon and 13 parameters for the sea quarks [106].

The first global fit to describe leading-order nuclear effects was the EKS98 nPDF [107]. The pion data collected by RHIC was later included in EPS08 [108], EPS09 [109], DSSZ [110] and nCTEQ15 [111] nPDFs which provided constraints to the gluon nPDF. We will focus on the latest nuclear PDF calculations which are the EPPS16 [112] and the nCTEQ15 [111] NLO nPDFs.

The EPPS16 nPDFs [112] are derived from a global analysis of nuclear data sets published in 2017 by the group of Eskola, Paakkinen, Paukkunen and Salgado (EPPS). The EPPS16 nPDF calculations update their previous EPS09 [109] global fits. EPPS16 includes five additional parameters compared to EPS09 to account for possible flavour dependence of the quark nuclear modifications. The EPPS16 global fits include the same data sets as EPS09 (charged-lepton-nucleus DIS data from SLAC, DY dilepton production from EMC proton-nucleus collisions and inclusive pion production from RHIC deuteron-nucleus collisions), as well as the CHORUS neutrino-nucleus DIS data, low-mass DY production from RHIC pion-nucleus collisions, and the results using dijet and electroweak boson production in LHC pPb collisions at $\sqrt{s_{\text{NN}}} = 5.02$ TeV. The addition of the new LHC, RHIC and CHORUS data into the global fit is not in tension with the previous EPS09 data sets, reassuring the validity of the universality of the nPDFs. Moreover, the inclusion of the CMS measurements of dijet production in pPb collisions at $\sqrt{s_{\text{NN}}} = 5.02$ TeV highly constrained the gluon nPDF. On the other hand, the LHC measurements of the electroweak boson production in pPb data was not able to further constrain the quark nPDF due to the limited statistical precision. The nuclear PDFs are parameterized in EPPS16 as:

$$f_i^{p/A}(x, Q^2) = R_i^A(x, Q^2) f_i^p(x, Q^2) \quad (4.8)$$

where $f_i^{p/A}$ represents the PDF of a proton bounded in a nucleus A, f_i^p is the free proton PDF and R_i^A is the corresponding nuclear modification. The EPPS16 nuclear modifications are derived using the NLO CT14 PDF as the free proton baseline. The parameters of R_i^A are determined in three regions: the shadowing region $x \rightarrow 0$, the antishadowing maximum point x_a and the EMC minimum point x_e . The dependence on the atomic mass A is parameterized along the three x regions in the following way:

$$R_i^A(x, Q_0^2) = R_i^{A_{\text{ref}}}(x, Q_0^2) \left(\frac{A}{A_{\text{ref}}} \right)^{\gamma_i [R_i^{A_{\text{ref}}}(x, Q_0^2) - 1]} \quad (4.9)$$

241 where Q_0 is the parameterization scale fixed at the charm pole mass (1.3 GeV), γ_i
 242 is a positive parameter and $A_{\text{ref}} = 12$. The Q^2 dependence above Q_0^2 is determined by
 243 solving the DGLAP parton evolution equations. The strong coupling constant evaluated
 244 at the Z boson mass is set to $\alpha_s(M_Z) = 0.118$. The EPPS16 nuclear modifications are
 245 parameterized in total by 20 parameters.

246 The nCTEQ15 nuclear PDF published by Kovarik et al. in 2016 was derived using the
 247 CTEQ framework at next-to-leading order. The nCTEQ15 nPDF global fits make use of
 248 charged-lepton DIS data, DY dilepton production and RHIC inclusive pion production. In
 249 contrast with EPPS16 where the nuclear modification factor $R_i^{p/A}$ is fitted, the nCTEQ15
 250 global analysis parametrizes the nuclear PDF $f_i^{p/A}$ directly (i.e. no free proton PDF is
 251 used as baseline). The nCTEQ nPDFs are parameterized as:

$$\begin{aligned}
 x f_i^{p/A}(x, Q_0) &= c_0 x^{c_1} (1-x)^{c_2} e^{c_3 x} (1 + e^{x_4} x)^{c_5} \\
 \frac{\bar{d}(x, Q_0)}{\bar{u}(x, Q_0)} &= c_0 x^{c_1} (1-x)^{c_2} + (1 + c_3 x)(1-x)^{c_4} \\
 s^{p/A}(x, Q_0) &= \bar{s}^{p/A}(x, Q_0) = \frac{\kappa(A)}{2} \left(\bar{u}^{p/A}(x, Q_0) + \bar{d}^{p/A}(x, Q_0) \right)
 \end{aligned} \tag{4.10}$$

252 where $f_i^{p/A}$ is defined for $i = (u_v, d_v, g, \bar{u} + \bar{d}, s + \bar{s}, s - \bar{s})$, $\kappa(A) = \left(c_{0,0}^{s+\bar{s}} + c_{0,1}^{s+\bar{s}} \left(1 - A^{-c_{0,2}^{s+\bar{s}}} \right) \right)$
 253 and the parameterization scale $Q_0 = 1.3$ GeV. The A-dependence of the nCTEQ15 nPDF
 254 is parameterized directly in the coefficients using $c_k(A) = c_{k,0} + c_{k,1} (1 - A^{-c_{k,2}})$, where
 255 $k = 1, \dots, 5$.

256 The nCTEQ15 global fits to the data sets are performed by minimizing the χ^2 . The
 257 nCTEQ15 fits are performed using 16 free parameters separated in: 7 gluon, 4 up valence
 258 quark, 3 down valence quark and 2 ($d + u$) antiquark parameters. Also, nCTEQ15 treat
 259 the light valence quark densities independently but it assume no flavour dependence of
 260 the light antiquark nuclear modifications. The nCTEQ15 calculations avoid fitting the low
 261 Q^2 and high x region $x > 0.7$ since this region is very difficult to model theoretically due
 262 to the presence of target mass corrections, large x resummation, nuclear off-shell effects
 263 and Fermi motion effects which steeply rise the parton densities when approaching $x = 1$.

264 The PDF uncertainties are determined using the Hessian matrix approach. The
 265 main idea of the Hessian method is that the distribution of the $\chi^2(\{a_i\})$ around its
 266 minimum $\chi^2(\{a_i^0\})$ can be approximately parameterized by a quadratic function of the
 267 n fitting parameters $\{a_i\}$ as $\chi^2(\{a_i\}) \approx \chi^2(\{a_i^0\}) + \sum_{i,j} y_i H_{i,j} y_j$ where $y_i = a_i - a_i^0$ and $H_{i,j} =$
 268 $(1/2)(d^2 \chi^2 / dy_i dy_j)_{a_i=a_i^0}$ is the Hessian matrix that encodes the impact of variations
 269 around each parameter. Since $H_{i,j}$ is a symmetric matrix, it has n orthogonal eigenvectors.
 270 The eigenvectors of $H_{i,j}$ are used to define a new basis $\{z_k\}$ which transform H into a

diagonal matrix. In order to compute the PDF uncertainties, the EPPS16 and nCTEQ15 calculations provide the PDF central set S_0 and the PDF error sets S_k^\pm defined in the $\{z_k\}$ coordinates. Each S_k^\pm is determined by evaluating the PDF on $\{z_k^\pm\}$ defined by varying upward/downward the parameter $\{z_k\}$ along the k-th eigenvector direction as:

$$S_k^\pm = f\left(z_k^0 \pm \sqrt{\frac{\Delta\chi^2}{\lambda_k}}\right) \quad (4.11)$$

where λ_k is the k-th eigenvalue of H and $\Delta\chi^2$ is the tolerance criterion defined at 90% confidence limit. In nCTEQ15 the tolerance is set to $\Delta\chi^2 = 35$ while in EPPS16 it is set to $\Delta\chi^2 = ??$. Using the PDF error sets, the PDF uncertainties can then be defined as:

$$\Delta O = \sqrt{\sum_i [\max_{\min} \{O(S_i^+) - O(S_i^0), O(S_i^-) - O(S_i^0), 0\}]^2} \quad (4.12)$$

To derive the correlation between two observables X and Y , one can use the cosine of the correlation angle define as:

$$\cos\phi[X, Y] = \frac{\sum_{i_{\text{PDF}}} (X_{i_{\text{PDF}}}^+ - X_{i_{\text{PDF}}}^-)}{(Y_{i_{\text{PDF}}}^+ - Y_{i_{\text{PDF}}}^-)} \sqrt{\sum_{j_{\text{PDF}}} (X_{j_{\text{PDF}}}^+ - X_{j_{\text{PDF}}}^-)^2} \sqrt{\sum_{k_{\text{PDF}}} (Y_{k_{\text{PDF}}}^+ - Y_{k_{\text{PDF}}}^-)^2} \quad (4.13)$$

where the observables are calculated over the upward/downward PDF error sets in each eigenvector direction (16 for nCTEQ15 and 20 for EPPS16). The main differences between the EPS09, EPPS16 and nCTEQ15 nuclear PDFs are summarized in Table 4.1.4.

4.1.5 Production of W bosons at LHC

The production of W bosons in hadronic collisions is accomplished through the process of quark-antiquark annihilation. The measurement of W boson production in pPb collisions at $\sqrt{s_{\text{NN}}} = 8.16$ TeV is performed in the semimuonic decay channel. At leading order (LO), the W boson hadroproduction to final state leptons is described by the Feynman diagram shown in Fig. 4.2.

In this thesis, the cross section of the W boson production is measured in pPb collisions as a function of muon pseudorapidity (η) considering muons with p_T larger than 25 GeV/c. The theoretical cross section can be derived using electroweak theory and the factorization theorem shown in Eq. (1.6). The W boson hadroproduction cross section has been calculated in Ref. [113], and the corresponding pPb LO differential cross section as a function of muon η , considering $\Gamma_W \ll M_W$, is:

nPDF	EPS09	EPPS16	nCTEQ15
Order	NLO	NLO	NLO
Fit	nuclear modification	nuclear modification	nuclear PDF
Baseline PDF	CT14	CTEQ6	
Free parameters	15	20	17
Data points	929	1811	708
EMC DY dileptons in p-A	Yes	Yes	Yes
RHIC pions in d-A	Yes	Yes	Yes
SLAC l^\pm -A DIS	Yes	Yes	Yes
CHORUS ν -A DIS	No	Yes	No
RHIC DY in π -A	No	Yes	No
LHC dijets in pPb	No	Yes	No
LHC weak bosons in pPb	No	Yes	No

Table 4.2: Summary of the information of EPS09, EPPS16 and nCTEQ15 nuclear PDFs.

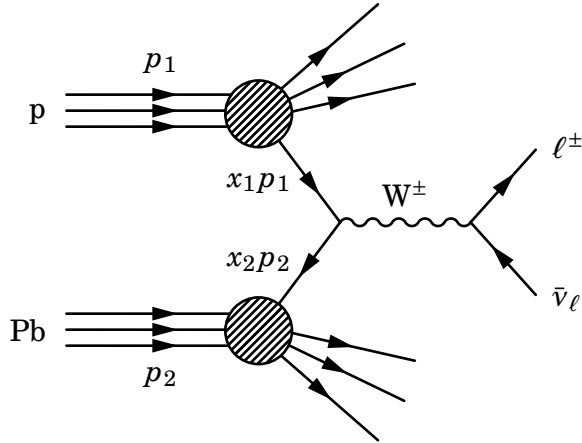


Figure 4.2: Feynman diagram of LO W boson production to final state leptons in pPb collisions

$$\begin{aligned}
\frac{d\sigma^{W^\pm}}{d\eta}(s_{NN}) \approx & \frac{\pi^2}{6M_W^5\Gamma_W} \left(\frac{\alpha_{em}}{\sin^2(\theta_W)} \right)^2 \int_{25}^{\text{inf}} dp_T \frac{p_T^3}{\sqrt{1-4p_T^2/M_W^2}} \sum_{i,j} \delta(e_{q_i} + e_{\bar{q}_j}, \pm 1) |V_{ij}^{\text{CKM}}|^2 \\
& \left\{ x_p^\pm q_i^p(x_p^+, Q^2) \cdot x_{Pb}^\mp \bar{q}_j^{\text{Pb}}(x_{Pb}^+, Q^2) + x_p^\pm \bar{q}_i^p(x_p^-, Q^2) \cdot x_{Pb}^\mp q_j^{\text{Pb}}(x_{Pb}^-, Q^2) + \right. \\
& \left. x_p^\mp q_i^p(x_p^-, Q^2) \cdot x_{Pb}^\pm \bar{q}_j^{\text{Pb}}(x_{Pb}^-, Q^2) + x_p^\mp \bar{q}_i^p(x_p^+, Q^2) \cdot x_{Pb}^\pm q_j^{\text{Pb}}(x_{Pb}^+, Q^2) \right\}
\end{aligned} \tag{4.14}$$

where α_{em} is the fine-structure constant, q^p is the free-proton quark PDF, q_i^{Pb} is the Pb nuclear quark PDF, and $Q \approx M_W$ is the momentum scale. The sum in Eq. (4.14) is performed over all quark flavours and the parton momentum fraction variables x_p and x_{Pb} are defined as [113]:

$$\begin{aligned}
x_p^\pm &= \frac{M_W}{\sqrt{s_{NN}}} e^\eta \left[\frac{1 \mp \sqrt{1-4p_T^2/M_W^2}}{2p_T/M_W} \right] \\
x_{Pb}^\pm &= \frac{M_W}{\sqrt{s_{NN}}} e^{-\eta} \left[\frac{1 \pm \sqrt{1-4p_T^2/M_W^2}}{2p_T/M_W} \right]
\end{aligned} \tag{4.15}$$

The cross sections of negative and positive charged leptons, shown in Eq. (4.14), are different due to parity violation and helicity conservation of weak decays. Since W^+ bosons couple to right-handed leptons while W^- couples to left-handed leptons, leptons are produced in the same direction as the W boson while antileptons are generated in the opposite direction. This is reflected in Eq. (4.15) where μ^- production is sensitive to slightly higher x than μ^+ production.

Multiple proton-proton and proton-neutron hard scatterings takes place during pPb collisions. In this case, the W bosons are mainly produced from interactions between the valence quarks and sea antiquarks of the nucleons. The dominant production modes of W^+ bosons correspond to up quark and down antiquark annihilation while for W^- bosons correspond to down quark and up antiquark annihilation. The annihilation between light quarks and heavier antiquarks is also possible but highly suppressed according to the CKM matrix elements. Therefore, the inclusive W boson cross section measured in pPb data is mostly sensitive to the proton and Pb-nucleus PDFs of light quarks and antiquarks.

In addition, the W boson cross sections can be compared between different beam energies. According to Arleo, Chapon and Paukkunen [113], at small enough x values, the

316 W boson cross section follows a power-like scaling as a function of s_{NN} , where Eq. (4.14)
 317 can be approximately reduced to:

$$\begin{aligned} \frac{d\sigma^{\text{W}^\pm}}{d\eta}(s_{\text{NN}}, \xi_p) &\approx (s_{\text{NN}})^\alpha \times F_{\text{p,Pb}}^\pm(\xi_p, p_T), \quad \eta > 0, \\ \frac{d\sigma^{\text{W}^\pm}}{d\eta}(s_{\text{NN}}, \xi_{\text{Pb}}) &\approx (s_{\text{NN}})^\alpha \times G_{\text{p,Pb}}^\pm(\xi_{\text{Pb}}, p_T), \quad \eta < 0 \end{aligned} \quad (4.16)$$

318 where α is the scaling parameter, and $\xi_p = (M_W/\sqrt{s_{\text{NN}}})e^{-\eta}$ and $\xi_{\text{Pb}} = (M_W/\sqrt{s_{\text{NN}}})e^\eta$
 319 are the x values at $p_T = M_W/2$ in the proton and Pb ion, respectively. Moreover, the
 320 functions $F_{\text{p,Pb}}^\pm$ and $G_{\text{p,Pb}}^\pm$ do not depend explicitly on s or η .

321 Furthermore, since the scaling parameter does not depend on the lepton pseudora-
 322 pidity or the charge of the W boson, the dependence on s_{NN} cancels in ratios of W boson
 323 cross sections. We can then measure asymmetries to improve the sensitivity to different
 324 aspects of the W boson production. Two of the most commonly used are the lepton charge
 325 asymmetry defined in Eq. (4.18) and the forward-backward ratio presented in Eq. (4.20).
 326 Thus, according to Eq. (4.16), the W boson asymmetries only depends on ξ_p and ξ_{Pb} for
 327 $|\eta| > 0.5 \ln(s_{\text{NN}}/M_W^2)$.

4.2 W boson production in pPb collisions at

$$\sqrt{s_{\text{NN}}} = 8.16 \text{ TeV}$$

This section presents the results of the analysis of the production of W bosons in pPb collisions at $\sqrt{s_{\text{NN}}} = 8.16 \text{ TeV}$ performed in the semi-muonic decay channel, using a data sample with integrated luminosity of $173.4 \pm 5.9 \text{ nb}^{-1}$ [114]. The W boson yields are extracted in the muon kinematic region defined by $p_{\text{T}}^{\mu} > 25 \text{ GeV}/c$ and $|\eta_{\text{lab}}^{\mu}| < 2.4$. The W boson differential cross sections, the muon charge asymmetry, and the muon forward-backward ratios are measured as a function of muon η_{CM} . The measurements are compared to PDF calculations both without and with including nuclear modifications, and also to results from other LHC experiments.

4.2.1 Observables

4.2.1.1 W boson cross sections

The differential $W \rightarrow \mu\nu_{\mu}$ cross sections are calculated by dividing the efficiency-corrected $W \rightarrow \mu\nu_{\mu}$ yields (N_{corr}) over the recorded integrated luminosity (\mathcal{L}) times the bin width ($\Delta\eta_{\text{CM}}$), as described below:

$$\frac{d\sigma^{\pm}}{d\eta_{\text{CM}}}(\eta_{\text{CM}}) = \frac{N_{\text{corr}}^{\pm}(\eta_{\text{CM}})}{\Delta\eta_{\text{CM}}\mathcal{L}} \quad (4.17)$$

The results of the production cross sections for $W^{+} \rightarrow \mu^{+}\nu_{\mu}$ and $W^{-} \rightarrow \mu^{-}\bar{\nu}_{\mu}$, as a function muon η_{CM} , are shown in Fig. 4.3. The vertical error bars represent the statistical uncertainties from the measured $W \rightarrow \mu\nu_{\mu}$ yields, while the brackets show the statistical and total systematic uncertainties summed in quadrature. The global integrated luminosity uncertainty of $\pm 3.4\%$ [114] is not shown.

The opposite trend seen between the W^{+} and W^{-} boson differential cross sections is expected from parity violation of the electroweak interaction. The W^{+} bosons decay to a right-handed antimuon boosted in the opposite direction, while the W^{-} bosons decay to a left-handed muon along the direction of the W^{-} boson. As a consequence, the μ^{+} and μ^{-} yields differ as a function of the muon η_{CM} .

4.2.1.2 Muon charge asymmetry

The muon charge asymmetry (C_{μ}) between $W^{-} \rightarrow \mu^{-}\bar{\nu}_{\mu}$ and $W^{+} \rightarrow \mu^{+}\nu_{\mu}$ processes and its corresponding uncertainty are defined in Eq. (4.18) and Eq. (4.19), respectively.

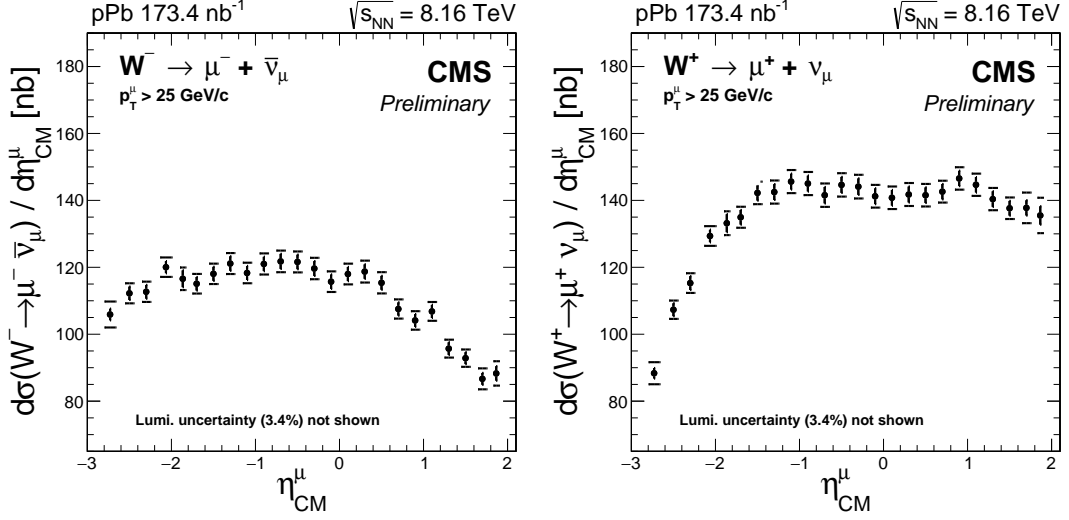


Figure 4.3: Production cross sections for $W^+ \rightarrow \mu^+ \nu_\mu$ (left) and $W^- \rightarrow \mu^- \bar{\nu}_\mu$ (right), as a function of the muon pseudorapidity in the center-of-mass frame. The brackets represent the statistical and systematic uncertainties summed in quadrature, while the error bars show the statistical uncertainties only. The global luminosity uncertainty of $\pm 3.4\%$ [114] is not shown.

$$C_\mu(\eta_{CM}) = \frac{N_{corr}^+(\eta_{CM}) - N_{corr}^-(\eta_{CM})}{N_{corr}^+(\eta_{CM}) + N_{corr}^-(\eta_{CM})} \quad (4.18)$$

$$\delta C_\mu(\eta_{CM}) = \left(\frac{2 \times N_{corr}^+(\eta_{CM}) \times N_{corr}^-(\eta_{CM})}{(N_{corr}^+(\eta_{CM}) + N_{corr}^-(\eta_{CM}))^2} \right) \times \sqrt{\left(\frac{\delta N_{corr}^+(\eta_{CM})}{N_{corr}^+(\eta_{CM})} \right)^2 + \left(\frac{\delta N_{corr}^-(\eta_{CM})}{N_{corr}^-(\eta_{CM})} \right)^2} \quad (4.19)$$

356 The uncertainties correlated in muon charge, such as the integrated luminosity
 357 uncertainty of 3.4% and the systematic components of the tag-and-probe correction
 358 uncertainties ($< 2.8\%$), cancel in the measurement of the muon charge asymmetry. The
 359 measured muon charge asymmetry is shown in Fig. 4.4 as a function muon η_{CM} .

360 4.2.1.3 Muon forward-backward ratios

361 The muon forward-backward ratio (R_{FB}) is defined as the ratio of the $W \rightarrow \mu \nu_\mu$ yields
 362 extracted in the forward η_{CM} bin divided by its backward counterpart. By convention,
 363 the forward region corresponds to the proton-going direction while the backward region
 364 corresponds to the Pb-going direction. The muon forward-backward ratio is measured
 365 for each muon charge separately, and also considering all muons. The R_{FB} is defined in
 366 Eq. (4.20) and its uncertainty is computed using Eq. (4.21).

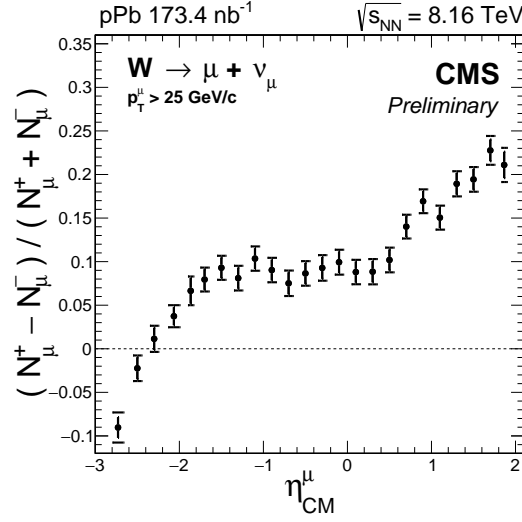


Figure 4.4: Muon charge asymmetry as a function of the muon pseudorapidity in the center-of-mass frame. The brackets represent the statistical and systematic uncertainties summed in quadrature, while the error bars show the statistical uncertainties only.

$$R_{FB}(\eta) = \frac{N_{corr}(+\eta_{CM})}{N_{corr}(-\eta_{CM})} \quad (4.20)$$

$$\delta R_{FB}(\eta_{CM}) = R_{FB}(\eta_{CM}) \times \sqrt{\left(\frac{\delta N_{corr}(+\eta_{CM})}{N_{corr}(+\eta_{CM})}\right)^2 + \left(\frac{\delta N_{corr}(-\eta_{CM})}{N_{corr}(-\eta_{CM})}\right)^2} \quad (4.21)$$

367 The results of the forward-backward ratio of all muons and the ratio for $W^- \rightarrow$
 368 $\mu^- \bar{\nu}_\mu$ and $W^+ \rightarrow \mu^+ \nu_\mu$ decays, are shown in Fig. 4.5. The uncertainties correlated in
 369 muon pseudorapidity, such as the integrated luminosity uncertainty of 3.4%, the event
 370 activity reweighing uncertainty and the systematic uncertainties due to the electroweak
 371 backgrounds, are strongly reduced.

372 4.2.2 Comparison with theoretical models

373 The measurements of the W boson production in pPb collisions at $\sqrt{s_{NN}} = 8.16$ TeV
 374 are compared to three NLO PDF calculations, one assuming no nuclear effects (CT14
 375 PDF [106]) and two including nuclear modifications (CT14+EPPS16 nPDF [112] and
 376 CT14+nCTEQ15 nPDF [111]). The NLO PDF calculations are produced using the parton-
 377 level Monte Carlo program MCFM [115]. The comparison between the PDF calculations
 378 and the data are shown in Fig. 4.6 for the W differential cross sections, in Fig. 4.7 for the
 379 muon charge asymmetry and in Fig. 4.8 for the muon forward backward ratios. In all

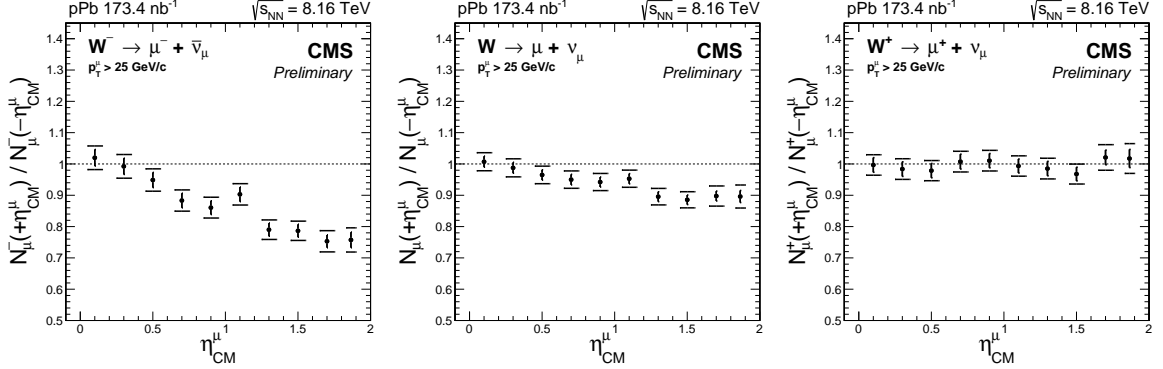


Figure 4.5: Forward-backward ratios, for the positive (left), all (middle) and negative (right) charged muons. The brackets represent the statistical and systematic uncertainties summed in quadrature, while the error bars show the statistical uncertainties only.

cases, the PDF calculations with (without) including nuclear modifications are displayed using dashed (continuous) lines and the corresponding PDF uncertainties are shown using hatched (filled) boxes.

As can be seen in Fig. 4.6, the W cross section measurements at forward rapidity favor the PDF calculations including nuclear modifications, while at backward rapidity all three PDF calculations are in good agreement with the data. Moreover, in the case of the muon charge asymmetry shown in Fig. 4.7, the results of the theory calculations derived using CT14 PDF only, and those including nuclear modifications described by EPPS16 nPDF, are in good agreement with the measurements while the CT14+nCTEQ15 nPDF calculations expect a slightly larger muon charge asymmetry in the most backward η_{CM} bins. Finally, from the ratios of muon yields at forward over backward η_{CM} displayed in Fig. 4.8, the nuclear PDF calculations describe much better the data compared to the free-nucleon PDF calculation. Considering the smaller size of the uncertainties compared to the theory uncertainties, the measurements have the potential to constrain the CT14+EPPS16 and the CT14+nCTEQ15 nPDF models.

In order to quantify the level of agreement between each PDF calculation and the measurements of the W boson production in pPb, a χ^2 test is performed. The χ^2 test is derived as described below:

$$\chi^2 = \sum_i \sum_j \left[(t(i) - d(i)) (cov_{data} + cov_{theory})^{-1} [i, j] (t(j) - d(j)) \right] \quad (4.22)$$

where $t(i)$ is the value of the observable predicted from the PDF calculation in bin i ,

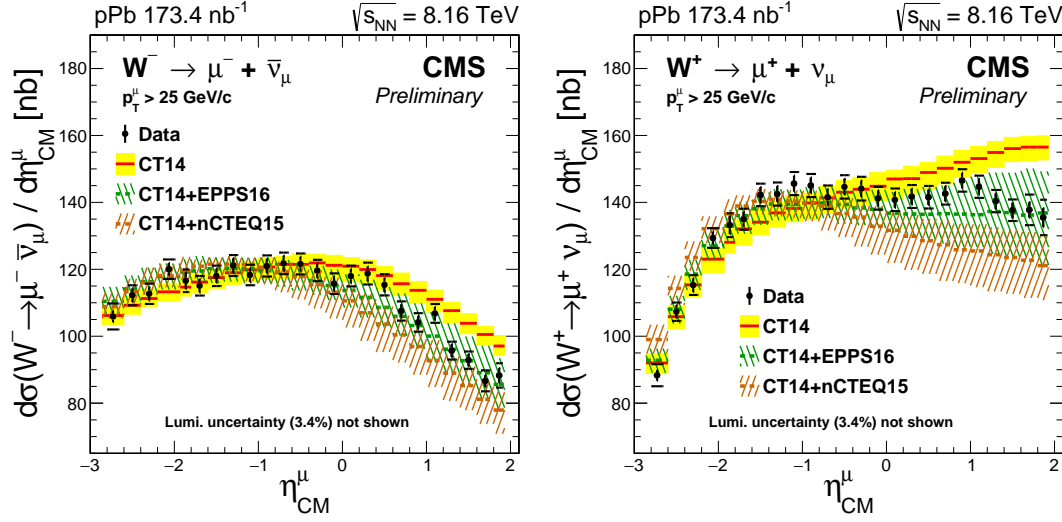


Figure 4.6: Differential cross sections for $W^+ \rightarrow \mu^+ \nu_\mu$ (left) and $W^- \rightarrow \mu^- \bar{\nu}_\mu$ (right), as a function of the muon pseudorapidity in the center-of-mass frame. Errors bars represent the statistical uncertainties, while the brackets represent the statistical and systematic uncertainties summed in quadrature. The global luminosity uncertainty of $\pm 3.4\%$ is not displayed. Theoretical predictions with (CT14+EPSS16 shown in dashed green line and CT14+nCTEQ15 shown in dashed brown line) and without (CT14, solid red line) PDF nuclear modifications are also shown, with the uncertainty bands. All theory uncertainty bands include PDF uncertainties.

$d(i)$ is the value of the observable measured in data in bin i , and $(cov_{data} + cov_{theory})^{-1}$ is the inverse of the sum of the covariance matrices extracted from the data and the model. This approach takes into account the bin-to-bin correlations in both muon charge and pseudorapidity. The outcome of the χ^2 statistical test derived using the CT14 PDF, the CT14+EPSS16 nPDF and the CT14+nCTEQ15 nPDF calculations are summarized in Table 4.3.

4.2.3 Comparison with other LHC experiments

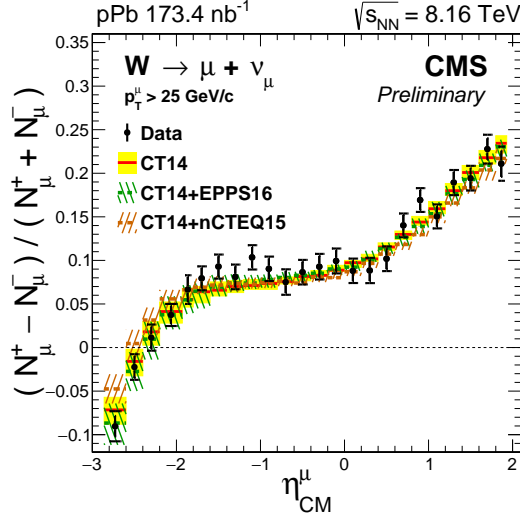


Figure 4.7: Muon charge asymmetry of $W \rightarrow \mu\nu_\mu$, given for each muon η_{CM} bin. Errors bars represent the statistical uncertainties, while the brackets represent the statistical and systematic uncertainties summed in quadrature. Theoretical predictions with (CT14+EPS16 shown in dashed green line and CT14+nCTEQ15 shown in dashed brown line) and without (CT14, solid red line) PDF nuclear modifications are also shown, with the uncertainty bands. All theory uncertainty bands include PDF uncertainties.

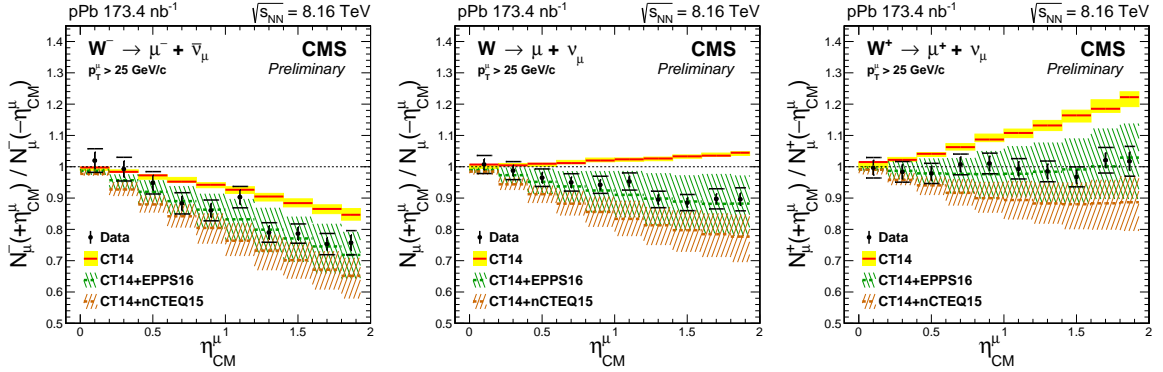


Figure 4.8: Forward-backward ratio of $W \rightarrow \mu\nu_\mu$, given for each muon η_{CM} bin separated in negative (left), all (middle) and positive (right) charged muons. Errors bars represent the statistical uncertainties, while the brackets represent the statistical and systematic uncertainties summed in quadrature. Theoretical predictions with (CT14+EPS16 shown in dashed green line and CT14+nCTEQ15 shown in dashed brown line) and without (CT14, solid red line) PDF nuclear modifications are also shown, with the uncertainty bands. All theory uncertainty bands include PDF uncertainties.

Observable	CT14			CT14+EPPS16			CT14+nCTEQ15		
	χ^2	ndf	Prob.(%)	χ^2	ndf	Prob.(%)	χ^2	ndf	Prob.(%)
$d\sigma(W \rightarrow \mu\nu_\mu)/d\eta_{CM}^\mu$	136	48	0	32	48	96	40	48	79
$(N_\mu^+ - N_\mu^-)/(N_\mu^+ + N_\mu^-)$	23	24	54	18	24	80	29	24	23
$N_\mu^\pm(+\eta_{CM}^\mu)/N_\mu^\pm(-\eta_{CM}^\mu)$	98	20	0	11	20	95	14	20	83
$N_\mu(+\eta_{CM}^\mu)/N_\mu(-\eta_{CM}^\mu)$	87	10	0	3	10	99	5	10	90

Table 4.3: Results of the χ^2 statistical test between the measurements and the theory calculations from the CT14 PDF, CT14+EPPS16 nPDF and CT14+nCTEQ15 nPDF models. The value of the χ^2 , the number of degrees of freedom (ndf) and the χ^2 probability (Prob.), are presented for the W differential cross sections, the muon charge asymmetry, the charged muon forward-backward ratios, and the forward-backward ratio of all muons, respectively.

CHAPTER



CONCLUSION

BIBLIOGRAPHY

- [1] E. Fermi, “Sulla quantizzazione del gas perfetto monoatomico”, *Rendiconti Lincei* **3** (1926) 145. [[Cited on page 3.](#)]
- [2] P. A. M. Dirac, “On the theory of quantum mechanics”, *Proceedings of the Royal Society of London A: Mathematical, Physical and Engineering Sciences* **112** (1926) 661,
<http://rspa.royalsocietypublishing.org/content/112/762/661.full.pdf>.
[[Cited on page 3.](#)]
- [3] W. Pauli, “Über den Zusammenhang des Abschlusses der Elektronengruppen im Atom mit der Komplexstruktur der Spektren”, *Zeitschrift für Physik* **31** (1925) 765. [[Cited on page 3.](#)]
- [4] S. N. Bose, “Plancks Gesetz und Lichtquantenhypothese”, *Zeitschrift für Physik* **26** (1924) 178. [[Cited on page 4.](#)]
- [5] A. Einstein, “Quantentheorie des einatomigen idealen Gases”, *Sitzungber. Kgl. Akad. Wiss.*, 1924 261. [[Cited on page 4.](#)]
- [6] **Belle** Collaboration, A. Bondar *et al.*, “Observation of two charged bottomonium-like resonances in $Y(5S)$ decays”, *Phys. Rev. Lett.* **108** (2012) 122001, arXiv:1110.2251. [[Cited on page 4.](#)]
- [7] **LHCb** Collaboration, R. Aaij *et al.*, “Observation of $J/\psi p$ Resonances Consistent with Pentaquark States in $\Lambda_b^0 \rightarrow J/\psi K^- p$ Decays”, *Phys. Rev. Lett.* **115** (2015) 072001, arXiv:1507.03414. [[Cited on page 4.](#)]
- [8] P. W. Higgs, “Broken Symmetries and the Masses of Gauge Bosons”, *Phys. Rev. Lett.* **13** (1964) 367. [[Cited on pages 5, 40, and 41.](#)]
- [9] F. Englert and R. Brout, “Broken Symmetry and the Mass of Gauge Vector Mesons”, *Phys. Rev. Lett.* **13** (1964) 321. [[Cited on pages 5, 40, and 41.](#)]

- [10] **CMS** Collaboration, S. Chatrchyan *et al.*, “Observation of a new boson at a mass of 125 GeV with the CMS experiment at the LHC”, *Phys. Lett. B* **716** (2012) 30, arXiv:1207.7235. [Cited on pages 5 and 40.]
- [11] **ATLAS** Collaboration, G. Aad *et al.*, “Observation of a new particle in the search for the Standard Model Higgs boson with the ATLAS detector at the LHC”, *Phys. Lett. B* **716** (2012) 1, arXiv:1207.7214. [Cited on pages 5 and 40.]
- [12] **Particle Data Group** Collaboration, C. Patrignani *et al.*, “Review of Particle Physics”, *Chin. Phys.* **C40** (2016), no. 10, 100001. [Cited on pages 5, 7, 8, 42, 43, 73, and 75.]
- [13] M. Gell-Mann, “The Eightfold Way: A Theory of strong interaction symmetry”, 1961. [Cited on page 5.]
- [14] Y. Ne’eman, “Derivation of strong interactions from a gauge invariance”, *Nucl. Phys.* **26** (1961) 222, [,34(1961)]. [Cited on page 5.]
- [15] M. Gell-Mann, “A Schematic Model of Baryons and Mesons”, *Phys. Lett.* **8** (1964) 214. [Cited on page 6.]
- [16] G. Zweig, “An SU(3) model for strong interaction symmetry and its breaking. Version 2”, in “DEVELOPMENTS IN THE QUARK THEORY OF HADRONS. VOL. 1. 1964 - 1978”, D. Lichtenberg and S. P. Rosen, eds., p. 22. 1964. [Cited on page 6.]
- [17] O. W. Greenberg, “Spin and Unitary Spin Independence in a Paraquark Model of Baryons and Mesons”, *Phys. Rev. Lett.* **13** (1964) 598. [Cited on page 6.]
- [18] H. Fritzsch, M. Gell-Mann, and H. Leutwyler, “Advantages of the Color Octet Gluon Picture”, *Phys. Lett. B* **47** (1973) 365. [Cited on page 6.]
- [19] G. ’t Hooft and M. J. G. Veltman, “Regularization and Renormalization of Gauge Fields”, *Nucl. Phys. B* **44** (1972) 189. [Cited on page 7.]
- [20] D. J. Gross and F. Wilczek, “Ultraviolet Behavior of Nonabelian Gauge Theories”, *Phys. Rev. Lett.* **30** (1973) 1343, [,271(1973)]. [Cited on page 8.]
- [21] H. D. Politzer, “Reliable Perturbative Results for Strong Interactions?”, *Phys. Rev. Lett.* **30** (1973) 1346, [,274(1973)]. [Cited on page 8.]

-
- [22] L. V. P. R. de Broglie, “Recherches sur la théorie des quanta”, *Annals Phys.* **2** (1925) 22. [[Cited on page 9.](#)]
 - [23] M. N. Chernodub, “Background magnetic field stabilizes QCD string against breaking”, arXiv:1001.0570. [[Cited on pages 10 and 75.](#)]
 - [24] J. D. Bjorken, “CURRENT ALGEBRA AT SMALL DISTANCES”, *Conf. Proc.* **670717** (1967) 55–81. [[Cited on page 10.](#)]
 - [25] G. Altarelli and G. Parisi, “Asymptotic Freedom in Parton Language”, *Nucl. Phys. B* **126** (1977) 298–318. [[Cited on page 11.](#)]
 - [26] Y. L. Dokshitzer, “Calculation of the Structure Functions for Deep Inelastic Scattering and e^+e^- Annihilation by Perturbation Theory in Quantum Chromodynamics.”, *Sov. Phys. JETP* **46** (1977) 641–653, [*Zh. Eksp. Teor. Fiz.* 73,1216(1977)]. [[Not cited.](#)]
 - [27] V. N. Gribov and L. N. Lipatov, “Deep inelastic $e p$ scattering in perturbation theory”, *Sov. J. Nucl. Phys.* **15** (1972) 438, [*Yad. Fiz.* 15,781(1972)]. [[Cited on page 11.](#)]
 - [28] **ZEUS** Collaboration, S. Chekanov *et al.*, “A ZEUS next-to-leading-order QCD analysis of data on deep inelastic scattering”, *Phys. Rev. D* **67** (2003) 012007, arXiv:hep-ex/0208023. [[Cited on pages 11, 12, and 75.](#)]
 - [29] R. Hagedorn, “Statistical thermodynamics of strong interactions at high energies”, *Nuovo Cimento, Suppl.* **3** (1965) 147. [[Cited on page 13.](#)]
 - [30] J. L. Kneur and A. Neveu, “ $\Lambda_{\overline{MS}}^{QCD}$ from Renormalization Group Optimized Perturbation”, *Phys. Rev. D* **85** (2012) 014005, arXiv:1108.3501. [[Cited on page 14.](#)]
 - [31] N. R. Council, “Nuclear physics: Exploring the heart of matter”, The National Academies Press, Washington, DC, 2013. [[Cited on pages 14, 17, 20, and 75.](#)]
 - [32] M. G. Alford, A. Schmitt, K. Rajagopal, and T. Schäfer, “Color superconductivity in dense quark matter”, *Rev. Mod. Phys.* **80** (2008) 1455, arXiv:0709.4635. [[Cited on page 14.](#)]
 - [33] H.-T. Ding, “Recent lattice QCD results and phase diagram of strongly interacting matter”, *Nucl. Phys. A* **931** (2014) 52, arXiv:1408.5236. [[Cited on page 15.](#)]

BIBLIOGRAPHY

- [34] A. Bazavov *et al.*, “Equation of state and QCD transition at finite temperature”, *Phys. Rev. D* **80** (2009) 014504, arXiv:0903.4379. [Cited on page 15.]
- [35] W. Scheid, H. Muller, and W. Greiner, “Nuclear Shock Waves in Heavy-Ion Collisions”, *Phys. Rev. Lett.* **32** (1974) 741. [Cited on page 15.]
- [36] E. Lofgren, “ACCELERATOR DIVISION ANNUAL REPORTS, 1 JULY 1972 12/31/1974”, 1975. [Cited on page 15.]
- [37] V. R. Pandharipande, D. Pines, and R. A. Smith, “Neutron star structure: theory, observation, and speculation.”, *Astrophys. J.* **208** (1976) 550. [Cited on page 15.]
- [38] T. L. Ainsworth, E. Baron, G. E. Brown, J. Cooperstein, and M. Prakash, “Equation of State of Dense Nuclear Matter”, *Nucl. Phys. A* **464** (1987) 740. [Cited on page 15.]
- [39] CERN, “New State of Matter created at CERN”, 2000. [Online; accessed June 11, 2018]. [Cited on page 16.]
- [40] **PHENIX, PHOBOS, STAR, BRAHMS** Collaboration, T. Ludlam and S. Aronson, “Hunting the quark gluon plasma”, 2005. [Cited on page 16.]
- [41] M. L. Miller, K. Reygers, S. J. Sanders, and P. Steinberg, “Glauber modeling in high energy nuclear collisions”, *Ann. Rev. Nucl. Part. Sci.* **57** (2007) 205, arXiv:nucl-ex/0701025. [Cited on page 18.]
- [42] U. W. Heinz, “The Strongly coupled quark-gluon plasma created at RHIC”, *J. Phys. A* **42** (2009) 214003, arXiv:0810.5529. [Cited on pages 22 and 75.]
- [43] R. Snellings, “Elliptic Flow: A Brief Review”, *New J. Phys.* **13** (2011) 055008, arXiv:1102.3010. [Cited on pages 22 and 23.]
- [44] P. Kovtun, D. T. Son, and A. O. Starinets, “Viscosity in strongly interacting quantum field theories from black hole physics”, *Phys. Rev. Lett.* **94** (2005) 111601, arXiv:hep-th/0405231. [Cited on page 23.]
- [45] J.-Y. Ollitrault, “Relativistic hydrodynamics for heavy-ion collisions”, *Eur. J. Phys.* **29** (2008) 275, arXiv:0708.2433. [Cited on page 23.]
- [46] P. Braun-Munzinger and J. Stachel, “The quest for the quark-gluon plasma”, *Nature* **448** (2007) 302. [Cited on pages 23 and 76.]

-
- [47] J. Rafelski and R. Hagedorn, “From Hadron Gas to Quark Matter. 2.”, in “International Symposium on Statistical Mechanics of Quarks and Hadrons Bielefeld, Germany, August 24-31, 1980”, pp. 253–272. 1980. [Cited on page 24.]
- [48] A. Capella, “Strangeness enhancement in heavy ion collisions”, *Phys. Lett. B* **364** (1995) 175, arXiv:hep-ph/9501331. [Cited on page 24.]
- [49] F. Becattini and G. Pettini, “Strange quark production in a statistical effective model”, *Phys. Rev. C* **67** (2003) 015205, arXiv:hep-ph/0204340. [Cited on page 24.]
- [50] J. Rafelski, “Strangeness as a signature of quark gluon plasma, CERN-Alice Summer Student Lecture”, 2011. [Online; accessed June 13, 2018]. [Cited on pages 25 and 76.]
- [51] C. Blume and C. Markert, “Strange hadron production in heavy ion collisions from SPS to RHIC”, *Prog. Part. Nucl. Phys.* **66** (2011) 834, arXiv:1105.2798. [Cited on page 24.]
- [52] A. Andronic, P. Braun-Munzinger, and J. Stachel, “Thermal hadron production in relativistic nuclear collisions: The Hadron mass spectrum, the horn, and the QCD phase transition”, *Phys. Lett. B* **673** (2009) 142, arXiv:0812.1186, [Erratum: *Phys. Lett. B* 678, 516 (2009)]. [Cited on pages 26 and 76.]
- [53] **ALICE** Collaboration, J. Adam *et al.*, “Enhanced production of multi-strange hadrons in high-multiplicity proton-proton collisions”, *Nature Phys.* **13** (2017) 535, arXiv:1606.07424. [Cited on page 24.]
- [54] M. Cacciari, G. P. Salam, and G. Soyez, “The Anti-k(t) jet clustering algorithm”, *JHEP* **04** (2008) 063, arXiv:0802.1189. [Cited on page 25.]
- [55] J. D. Bjorken, “Energy Loss of Energetic Partons in Quark - Gluon Plasma: Possible Extinction of High p(t) Jets in Hadron - Hadron Collisions”, 1982. [Cited on page 26.]
- [56] A. P. S. . A. Stonebraker, “Sketch of jet production in proton-proton and heavy-ion collisions”, 2014. [Online; accessed June 8, 2018]. [Cited on pages 27 and 76.]
- [57] **ATLAS** Collaboration, G. Aad *et al.*, “Observation of a Centrality-Dependent Dijet Asymmetry in Lead-Lead Collisions at $\sqrt{s_{NN}} = 2.77$ TeV with the ATLAS Detector

- at the LHC”, *Phys. Rev. Lett.* **105** (2010) 252303, arXiv:1011.6182. [Cited on pages 28 and 76.]
- [58] H. S. Chung, J. Lee, and D. Kang, “Cornell Potential Parameters for S-wave Heavy Quarkonia”, *J. Korean Phys. Soc.* **52** (2008) 1151, arXiv:0803.3116. [Cited on page 28.]
- [59] T. Matsui and H. Satz, “ J/ψ Suppression by Quark-Gluon Plasma Formation”, *Phys. Lett. B* **178** (1986) 416. [Cited on page 29.]
- [60] CMS Collaboration, A. M. Sirunyan *et al.*, “Suppression of Excited Υ States Relative to the Ground State in Pb-Pb Collisions at $\sqrt{s_{NN}}=5.02$ TeV”, *Phys. Rev. Lett.* **120** (2018), no. 14, 142301, arXiv:1706.05984. [Cited on pages 30 and 76.]
- [61] NA50 Collaboration, M. C. Abreu *et al.*, “Anomalous J/ψ suppression in Pb-Pb interactions at 158 GeV/c per nucleon”, *Phys. Lett. B* **410** (1997) 337. [Cited on page 29.]
- [62] NA50 Collaboration, B. Alessandro *et al.*, “A New measurement of J/ψ suppression in Pb-Pb collisions at 158-GeV per nucleon”, *Eur. Phys. J. C* **39** (2005) 335, arXiv:hep-ex/0412036. [Cited on page 29.]
- [63] L. Yan, P. Zhuang, and N. Xu, “Competition between J/ψ suppression and regeneration in quark-gluon plasma”, *Phys. Rev. Lett.* **97** (2006) 232301, arXiv:nucl-th/0608010. [Cited on page 29.]
- [64] ALICE Collaboration, B. B. Abelev *et al.*, “Centrality, rapidity and transverse momentum dependence of J/ψ suppression in Pb-Pb collisions at $\sqrt{s_{NN}}=2.76$ TeV”, *Phys. Lett. B* **734** (2014) 314–327, arXiv:1311.0214. [Cited on pages 31 and 76.]
- [65] CMS Collaboration, S. Chatrchyan *et al.*, “Study of Z production in PbPb and pp collisions at $\sqrt{s_{NN}} = 2.76$ TeV in the dimuon and dielectron decay channels”, *JHEP* **03** (2015) 022, arXiv:1410.4825. [Cited on pages 32 and 77.]
- [66] CMS Collaboration, V. Khachatryan *et al.*, “Study of W boson production in pPb collisions at $\sqrt{s_{NN}} = 5.02$ TeV”, *Phys. Lett. B* **750** (2015) 565–586, arXiv:1503.05825. [Cited on page 37.]
- [67] ALICE Collaboration, K. Senosi, “Measurement of W-boson production in p-Pb collisions at the LHC with ALICE”, *PoS Bormio2015* (2015) 042, arXiv:1511.06398. [Cited on page 37.]

- [68] **ATLAS** Collaboration, M. Dumanfçifá, “W and Z boson production in 5.02 TeV pp and p +Pb collisions with the ATLAS detector”, *Nucl. Part. Phys. Proc.* **289-290** (2017) 193–196, arXiv:1704.00298. [[Cited on page 37.](#)]
- [69] E. Rutherford, “Uranium radiation and the electrical conduction produced by it”, *Philos. Mag.* **47** (1899) 109. [[Cited on page 38.](#)]
- [70] J. Chadwick, “Intensitätsverteilung im magnetischen Spektrum von β -Strahlen von Radium B+C”, *Verhandlungen der deutschen physikalischen Gesellschaft* **16** (1914) 383. [[Cited on page 38.](#)]
- [71] J. Chadwick and C. D. Ellis, “A Preliminary Investigation of the Intensity Distribution in the β -Ray Spectra of Radium B and C”, *Proceedings of the Cambridge Philosophical Society* **21** (1922) 274. [[Cited on page 38.](#)]
- [72] W. Pauli, “Fünf Arbeiten zum Ausschliessungsprinzip und zum Neutrino”, Wissenschaftliche Buchgesellschaft, [Abt. Verlag], 1977. [[Cited on page 38.](#)]
- [73] K. Winter, “Neutrino physics”, Cambridge University Press, 1991. [[Cited on page 38.](#)]
- [74] J. Chadwick, “Possible Existence of a Neutron”, *Nature* **129** (1932) 312. [[Cited on page 38.](#)]
- [75] E. Fermi, “Collected Papers of Enrico Fermi”, University of Chicago Press, 1965. [[Cited on page 38.](#)]
- [76] E. Fermi, “Versuch einer Theorie der β -Strahlen. I”, *Zeitschrift für Physik* **88** (1934) 161. [[Cited on page 38.](#)]
- [77] T. D. Lee and C. N. Yang, “Question of Parity Conservation in Weak Interactions”, *Phys. Rev.* **104** (1956) 254. [[Cited on page 39.](#)]
- [78] C. S. Wu, E. Ambler, R. W. Hayward, D. D. Hoppes, and R. P. Hudson, “Experimental Test of Parity Conservation in Beta Decay”, *Phys. Rev.* **105** (1957) 1413. [[Cited on page 39.](#)]
- [79] M. Goldhaber, L. Grodzins, and A. W. Sunyar, “Helicity of Neutrinos”, *Phys. Rev.* **109** (1958) 1015. [[Cited on page 39.](#)]

BIBLIOGRAPHY

- [80] E. C. G. Sudarshan and R. E. Marshak, “Origin of the Universal V,Ä theory”, *AIP Conf. Proc.* **300** (1994) 110, [,0001(1984)]. [[Cited on page 39.](#)]
- [81] J. H. Christenson, J. W. Cronin, V. L. Fitch, and R. Turlay, “Evidence for the 2π Decay of the K_2^0 Meson”, *Phys. Rev. Lett.* **13** (1964) 138–140. [[Cited on page 39.](#)]
- [82] M. Kobayashi and T. Maskawa, “CP Violation in the Renormalizable Theory of Weak Interaction”, *Prog. Theor. Phys.* **49** (1973) 652–657. [[Cited on page 39.](#)]
- [83] N. Cabibbo, “Unitary Symmetry and Leptonic Decays”, *Phys. Rev. Lett.* **10** (1963) 531–533, [,648(1963)]. [[Cited on page 39.](#)]
- [84] S. W. Herb *et al.*, “Observation of a Dimuon Resonance at 9.5-GeV in 400-GeV Proton-Nucleus Collisions”, *Phys. Rev. Lett.* **39** (1977) 252–255. [[Cited on page 39.](#)]
- [85] **CDF** Collaboration, F. Abe *et al.*, “Observation of top quark production in $\bar{p}p$ collisions”, *Phys. Rev. Lett.* **74** (1995) 2626–2631, arXiv:hep-ex/9503002. [[Cited on page 39.](#)]
- [86] P. A. M. Dirac, “The Principles of Quantum Mechanics”, Clarendon Press, 1930. [[Cited on page 39.](#)]
- [87] S. L. Glashow, “The renormalizability of vector meson interactions”, *Nucl. Phys.* **10** (1959) 107. [[Cited on pages 39 and 41.](#)]
- [88] S. Weinberg, “A Model of Leptons”, *Phys. Rev. Lett.* **19** (1967) 1264. [[Cited on page 39.](#)]
- [89] A. Salam, “Weak and Electromagnetic Interactions”, *Conf. Proc. C* **680519** (1968) 367. [[Cited on pages 39 and 41.](#)]
- [90] N. M. A. 2014, “The Nobel Prize in Physics 1979”.
http://www.nobelprize.org/nobel_prizes/physics/laureates/1979/, 2018.
Accessed: 2018-05-23. [[Cited on page 39.](#)]
- [91] G. t. Hooft, “Renormalizable Lagrangians for massive Yang-Mills fields”, *Nuclear Physics B* **35** (1971) 167. [[Cited on page 40.](#)]
- [92] G. t. Hooft and M. Veltman, “Regularization and renormalization of gauge fields”, *Nuclear Physics B* **44** (1972) 189. [[Cited on page 40.](#)]

- [93] C. Rubbia, P. McIntyre, and D. Cline, *Producing Massive Neutral Intermediate Vector Bosons with Existing Accelerators*, pp. 683–687. Vieweg+Teubner Verlag, Wiesbaden, 1977. [[Cited on page 40.](#)]
- [94] S. van der Meer, “Stochastic damping of betatron oscillations in the ISR”, Tech. Rep. CERN-ISR-PO-72-31. ISR-PO-72-31, CERN, Geneva, Aug 1972. [[Cited on page 40.](#)]
- [95] G. Arnison *et al.*, “Experimental observation of isolated large transverse energy electrons with associated missing energy at $\sqrt{s}=540$ GeV”, *Phys. Lett. B* **122** (1983) 103. [[Cited on page 40.](#)]
- [96] M. Banner *et al.*, “Observation of single isolated electrons of high transverse momentum in events with missing transverse energy at the CERN pp collider”, *Phys. Lett. B* **122** (1983) 476. [[Cited on page 40.](#)]
- [97] **UA1 Collaboration**, G. Arnison *et al.*, “Experimental Observation of Lepton Pairs of Invariant Mass Around 95-GeV/c² at the CERN SPS Collider”, *Phys. Lett. B* **126** (1983) 398, [,7.55(1983)]. [[Cited on page 40.](#)]
- [98] **UA2 Collaboration**, P. Bagnaia *et al.*, “Evidence for $Z^0 \rightarrow e^+ e^-$ at the CERN anti-p p Collider”, *Phys. Lett. B* **129** (1983) 130, [,7.69(1983)]. [[Cited on page 40.](#)]
- [99] N. M. A. 2014, “The Nobel Prize in Physics 1984”.
http://www.nobelprize.org/nobel_prizes/physics/laureates/1984/, 2018.
Accessed: 2018-05-23. [[Cited on page 40.](#)]
- [100] S. Myers, “The LEP Collider, from design to approval and commissioning”, CERN, Geneva, 1991. Delivered at CERN, 26 Nov 1990. [[Cited on page 40.](#)]
- [101] **DØ Collaboration**, V. M. Abazov *et al.*, “Improved W boson mass measurement with the DØ detector”, *Phys. Rev. D* **66** Jul (2002) 012001. [[Cited on page 40.](#)]
- [102] R. R. Wilson, “The Tevatron”, *Phys. Today* **30** (1977) 23. [[Cited on page 40.](#)]
- [103] **European Muon Collaboration**, J. J. Aubert *et al.*, “The ratio of the nucleon structure functions F_2^n for iron and deuterium”, *Phys. Lett. B* **123** (1983) 275–278. [[Cited on page 44.](#)]

- [104] **European Muon** Collaboration, M. Arneodo *et al.*, “Shadowing in Deep Inelastic Muon Scattering from Nuclear Targets”, *Phys. Lett. B* **211** (1988) 493–499. [[Cited on page 44.](#)]
- [105] **New Muon** Collaboration, D. o. Allasia, “Inelastic j/ψ production in deep inelastic scattering from hydrogen and deuterium and the gluon distribution of free nucleons”, *Physics Letters B* **258** (1991), no. 3, 493 – 498. [[Cited on page 44.](#)]
- [106] S. Dulat, T.-J. Hou, J. Gao, M. Guzzi, J. Huston, P. Nadolsky, J. Pumplin, C. Schmidt, D. Stump, and C. P. Yuan, “New parton distribution functions from a global analysis of quantum chromodynamics”, *Phys. Rev.* **D93** (2016), no. 3, 033006, [arXiv:1506.07443](#). [[Cited on pages 44, 45, and 53.](#)]
- [107] K. J. Eskola, V. J. Kolhinen, and C. A. Salgado, “The Scale dependent nuclear effects in parton distributions for practical applications”, *Eur. Phys. J. C* **9** (1999) 61–68, [arXiv:hep-ph/9807297](#). [[Cited on page 45.](#)]
- [108] K. J. Eskola, H. Paukkunen, and C. A. Salgado, “An Improved global analysis of nuclear parton distribution functions including RHIC data”, *JHEP* **07** (2008) 102, [arXiv:0802.0139](#). [[Cited on page 45.](#)]
- [109] K. J. Eskola, H. Paukkunen, and C. A. Salgado, “EPS09: A new generation of NLO and LO nuclear parton distribution functions”, *JHEP* **04** (2009) 065, [arXiv:0902.4154](#). [[Cited on page 45.](#)]
- [110] D. de Florian, R. Sassot, P. Zurita, and M. Stratmann, “Global Analysis of Nuclear Parton Distributions”, *Phys. Rev. D* **85** (2012) 074028, [arXiv:1112.6324](#). [[Cited on page 45.](#)]
- [111] K. Kovarik *et al.*, “nCTEQ15 - Global analysis of nuclear parton distributions with uncertainties in the CTEQ framework”, *Phys. Rev. D* **93** (2016), no. 8, 085037, [arXiv:1509.00792](#). [[Cited on pages 45 and 53.](#)]
- [112] K. J. Eskola, P. Paakkinen, H. Paukkunen, and C. A. Salgado, “EPPS16: Nuclear parton distributions with LHC data”, *Eur. Phys. J. C* **77** (2017), no. 3, 163, [arXiv:1612.05741](#). [[Cited on pages 45 and 53.](#)]
- [113] F. Arleo, É. Chapon, and H. Paukkunen, “Scaling properties of inclusive W^\pm production at hadron colliders”, *Eur. Phys. J. C* **76** (2016), no. 4, 214, [arXiv:1509.03993](#). [[Cited on pages 47 and 49.](#)]

- [114] **CMS Collaboration** Collaboration, “Luminosity calibration for the pPb/Pbp 2016 runs”, Tech. Rep. CMS-LUM-AN-17-002, CERN, Geneva, 2017. [[Cited on pages 51, 52, and 77.](#)]
- [115] J. M. Campbell and R. K. Ellis, “MCFM for the Tevatron and the LHC”, *Nucl. Phys. Proc. Suppl.* **205-206** (2010) 10–15, arXiv:1007.3492. [[Cited on page 53.](#)]

LIST OF TABLES

1.1	Basic properties of quarks, leptons and bosons from the SM. The table includes the mass, electric charge, spin and type of interactions of each particle. The values are taken from Ref. [12]	5
4.1	Experimental values of the mass, width and branching fractions of weak bosons extracted from the PDG [12].	43
4.2	Summary of the information of EPS09, EPPS16 and nCTEQ15 nuclear PDFs.	48
4.3	Results of the χ^2 statistical test between the measurements and the theory calculations from the CT14 PDF, CT14+EPPS16 nPDF and CT14+nCTEQ15 nPDF models. The value of the χ^2 , the number of degrees of freedom (ndf) and the χ^2 probability (Prob.), are presented for the W differential cross sections, the muon charge asymmetry, the charged muon forward-backward ratios, and the forward-backward ratio of all muons, respectively.	57

TABLE

Page

LIST OF FIGURES

1.1	Feynman diagrams of the QCD vertices for quark-gluon coupling (left), triple gluon self-coupling (middle) and quadri gluon self-coupling (right).	7
1.2	Feynman diagrams of 1-loop contributions to pQCD.	7
1.3	Summary of measurements of α_s as a function of the energy scale Q . Figure taken from the PDG [12]	8
1.4	Sketch of the gluon string breaking between a quark Q and an anti-quark \bar{Q} due to $q\bar{q}$ pair creation. Figure taken from Ref. [23]	10
1.5	Feynman diagram of deep inelastic scattering of electrons against protons . .	12
1.6	NLO QCD fits to the to the ZEUS F_2 structure function data from 1996, 1997 and proton fixed-target at HERA. The error bands of the fit represent the total experimental uncertainty from both correlated and uncorrelated sources. Figure taken from Ref. [28]	12
1.7	Feynman diagram of neutral charged Drell-Yan process	13
1.8	Schematic of the QCD phase diagram for nuclear matter. The solid lines show the phase boundaries and the solid circle represents the critical point. Figure taken from Ref. [31]	14
1.9	Illustration of two nucleus with impact parameter b before (left) and after (right) colliding. Figure taken from Ref. [31]	17
1.10	Schematic representation of the optical Glauber model geometry.	18
1.11	Schematic sketch of the evolution of a relativistic heavy ion collision. The wavy lines represent photons while the arrows correspond to jets. Figure taken from Ref. [31]	20
1.12	Sketch of the deformed medium and the elliptic flow produced in non-central heavy-ion collisions. Figure taken from Ref. [42]	22

1.13	Elliptic flow distribution of as a function of transverse momentum for π^\pm mesons, K_s^0 mesons, antiprotons and Λ baryons measured by STAR collaboration in Au-Au collisions at $\sqrt{s_{NN}} = 200$ GeV. The results are compared with relativistic hydrodynamic calculations. Figure taken from Ref. [46]	23
1.14	Sketch of the production of strange hadrons via gluon fusion in the QGP. Figure taken from Ref. [50]	25
1.15	Energy distribution of the relative production ratios K^+/π^+ and Λ/π^- at mid-rapidity measured at AGS (E802, E866, E895, E896) and SPS (NA44, NA49, NA57) in central Pb-Pb collisions, and at RHIC (STAR, PHENIX) in central Au-Au collisions. The solid line is the result of a statistical model calculation. The dotted line shows the K^+/π^+ ratio including the additional effect of higher mass resonances. The dashed lines show the energy dependence of the temperature (upper panel) and baryonic density (lower panel). Figure taken from Ref. [52]	26
1.16	Sketch of the production mechanism of two jets in proton-proton (top) and heavy-ions (bottom) collisions. Figure taken from Ref. [56]	27
1.17	Dijet asymmetry measured by the ATLAS collaboration in lead-lead collisions at $\sqrt{s_{NN}} = 2.76$ TeV (points) and proton-proton collisions at $\sqrt{s} = 7$ TeV (open circles). The top panel shows the dijet asymmetry distributions and unquenched HIJING with superimposed PYTHIA dijets (solid yellow histograms), as a function of collision centrality. The bottom panel shows the distribution of the azimuthal angle between the two jets $\Delta\phi$, for data and HIJING+PYTHIA, also as a function of centrality. Figure taken from Ref. [57]	28
1.18	Dimuon invariant mass distribution measured by the CMS collaboration in Pb-Pb collisions at $\sqrt{s_{NN}} = 5.02$ TeV. The total fit (solid blue line), the background component (dot-dashed blue line) and the individual $\Upsilon(1S)$, $\Upsilon(2S)$ and $\Upsilon(3S)$ mass peaks (dotted gray lines) are shown. The dashed red line represents the p-p signal shapes added on top of the Pb-Pb background and normalized to the $\Upsilon(1S)$ mass peak in Pb-Pb. Figure taken from Ref. [60]	30
1.19	Nuclear modification factor of J/ψ meson as a function of transverse momentum measured by the ALICE collaboration in the 0% – 20% most central Pb-Pb collisions at $\sqrt{s_{NN}} = 2.76$ TeV compared to results from the PHENIX collaboration measured in the 0% – 20% most central Au-Au collisions at $\sqrt{s_{NN}} = 200$ GeV. Figure taken from Ref. [64]	31

1.20	Nuclear modification factor R_{AA} of $Z \rightarrow e^+e^-$ (blue squares) and $Z \rightarrow \mu^+\mu^-$ (red circles) events as a function of the number of participants measured by the CMS collaboration in Pb-Pb collisions at $\sqrt{s_{NN}} = 2.56$ TeV. The open points represent the centrality-integrated R_{AA} and the vertical lines (boxes) correspond to statistical (systematic) uncertainties. The grey bar at $R_{AA} = 1$ represents the uncertainty of the luminosity determined in proton-proton collisions. Figure taken from Ref. [65]	32
4.1	Feynman diagram of the decay modes of W^+ (left) and W^- (right) bosons to fermions.	43
4.2	Feynman diagram of LO W boson production to final state leptons in pPb collisions	48
4.3	Production cross sections for $W^+ \rightarrow \mu^+\nu_\mu$ (left) and $W^- \rightarrow \mu^-\bar{\nu}_\mu$ (right), as a function of the muon pseudorapidity in the center-of-mass frame. The brackets represent the statistical and systematic uncertainties summed in quadrature, while the error bars show the statistical uncertainties only. The global luminosity uncertainty of $\pm 3.4\%$ [114] is not shown.	52
4.4	Muon charge asymmetry as a function of the muon pseudorapidity in the center-of-mass frame. The brackets represent the statistical and systematic uncertainties summed in quadrature, while the error bars show the statistical uncertainties only.	53
4.5	Forward-backward ratios, for the positive (left), all (middle) and negative (right) charged muons. The brackets represent the statistical and systematic uncertainties summed in quadrature, while the error bars show the statistical uncertainties only.	54
4.6	Differential cross sections for $W^+ \rightarrow \mu^+\nu_\mu$ (left) and $W^- \rightarrow \mu^-\bar{\nu}_\mu$ (right), as a function of the muon pseudorapidity in the center-of-mass frame. Errors bars represent the statistical uncertainties, while the brackets represent the statistical and systematic uncertainties summed in quadrature. The global luminosity uncertainty of $\pm 3.4\%$ is not displayed. Theoretical predictions with (CT14+EPPS16 shown in dashed green line and CT14+nCTEQ15 shown in dashed brown line) and without (CT14, solid red line) PDF nuclear modifications are also shown, with the uncertainty bands. All theory uncertainty bands include PDF uncertainties.	55

- 4.7 Muon charge asymmetry of $W \rightarrow \mu\nu_\mu$, given for each muon η_{CM} bin. Errors bars represent the statistical uncertainties, while the brackets represent the statistical and systematic uncertainties summed in quadrature. Theoretical predictions with (CT14+EPPS16 shown in dashed green line and CT14+nCTEQ15 shown in dashed brown line) and without (CT14, solid red line) PDF nuclear modifications are also shown, with the uncertainty bands. All theory uncertainty bands include PDF uncertainties. 56
- 4.8 Forward-backward ratio of $W \rightarrow \mu\nu_\mu$, given for each muon η_{CM} bin separated in negative (left), all (middle) and positive (right) charged muons. Errors bars represent the statistical uncertainties, while the brackets represent the statistical and systematic uncertainties summed in quadrature. Theoretical predictions with (CT14+EPPS16 shown in dashed green line and CT14+nCTEQ15 shown in dashed brown line) and without (CT14, solid red line) PDF nuclear modifications are also shown, with the uncertainty bands. All theory uncertainty bands include PDF uncertainties. 56

FIGURE**Page**